Holocene internal shortening within the northwest Sub-Himalaya: Out-of-sequence faulting of the Jwalamukhi Thrust, India

Saptarshi Dey[1], Rasmus C. Thiede[1], Taylor F. Schildgen[1,2], Hella Wittmann[2], Bodo Bookhagen[1], Dirk Scherler[2,3], and Manfred R. Strecker[1]
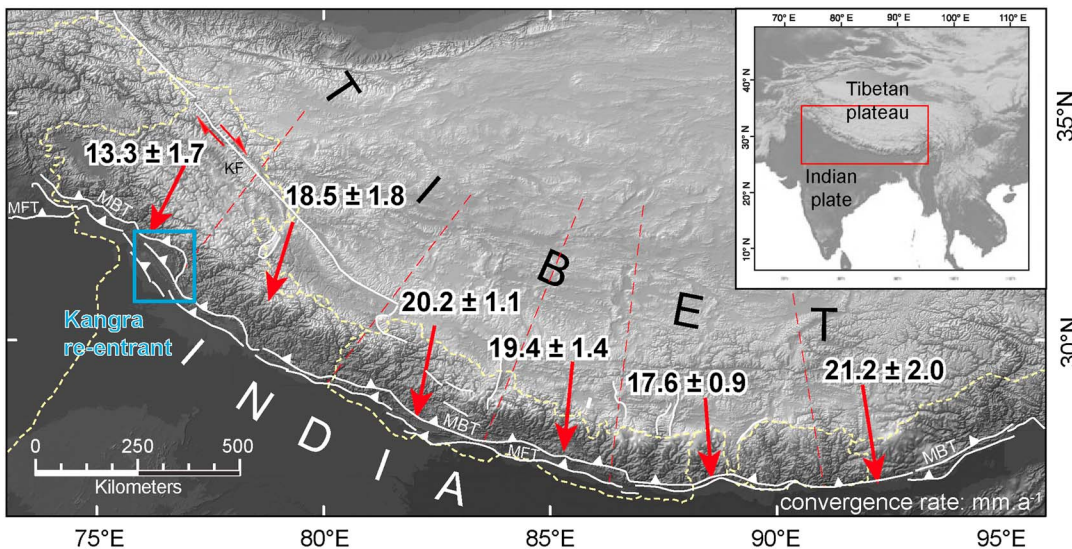
[1]Institut für Erd und Umweltwissenschaften, Universität Potsdam, Potsdam, Germany, [2]Helmholtz Zentrum Potsdam, Deutsches GeoForschungsZentrum GFZ, Potsdam, Germany, [3]Institute of Geological Sciences, Freie Universität Berlin, Berlin, Germany

Abstract The southernmost thrust of the Himalayan orogenic wedge that separates the foreland from the orogen, the Main Frontal Thrust, is thought to accommodate most of the ongoing crustal shortening in the Sub-Himalaya. Steepened longitudinal river profile segments, terrace offsets, and back-tilted fluvial terraces within the Kangra reentrant of the NW Sub-Himalaya suggest Holocene activity of the Jwalamukhi Thrust (JMT) and other thrust faults that may be associated with strain partitioning along the toe of the Himalayan wedge. To assess the shortening accommodated by the JMT, we combine morphometric terrain analyses with in situ ^{10}Be-based surface-exposure dating of the deformed terraces. Incision into upper Pleistocene sediments within the Kangra Basin created two late Pleistocene terrace levels (T1 and T2). Subsequent early Holocene aggradation shortly before ~10 ka was followed by episodic reincision, which created four cut-and-fill terrace levels, the oldest of which (T3) was formed at 10.1 ± 0.9 ka. A vertical offset of 44 ± 5 m of terrace T3 across the JMT indicates a shortening rate of 5.6 ± 0.8 to 7.5 ± 1.1 mm a^{-1} over the last ~10 ka. This result suggests that thrusting along the JMT accommodates 40–60% of the total Sub-Himalayan shortening in the Kangra reentrant over the Holocene. We speculate that this out-of-sequence shortening may have been triggered or at least enhanced by late Pleistocene and Holocene erosion of sediments from the Kangra Basin.

1. Introduction

The Himalaya is a tectonically active mountain belt resulting from ongoing collision between the northward moving, underthrusting Indian plate and the Eurasian plate [*Gansser,* 1964]. The vertical and lateral growth of the Himalaya has been accommodated by several major south verging thrust systems. From north to south, these include the Main Central Thrust (MCT), the Main Boundary Thrust (MBT), and the Main Frontal Thrust (MFT) [*Gansser,* 1964; *DeCelles et al.,* 2001]. All of these north dipping structures are rooted in the basal décollement, the Main Himalayan Thrust (MHT) [*Ni and Barazangi*, 1984; *Nábělek et al.,* 2009]. These thrust systems also define the regional morphotectonic sectors of the orogen: the Higher Himalaya in the hanging wall of the MCT, the Lesser Himalaya between the MCT and the MBT, and the Sub-Himalaya between the MBT and the southernmost MFT [*Gansser*, 1964]. Although these thrust systems have propagated southward in an overall in-sequence pattern, some out-of-sequence deformation has been reported. *Wobus et al.* [2005] proposed active out-of-sequence thrusting along the region known as the physiographic transition, south of the MCT in central Nepal. Out-of-sequence faults have also been reported by *Mukul et al.* [2007] in the Darjeeling Sub-Himalaya, by *Thakur et al.* [2007] between the MBT and the MFT near Dehradun, and by *Powers et al.* [1998] in the Kangra reentrant of the NW Himalaya.

The 40 to 50 mm a^{-1} convergence between the Indian and Eurasian plates is partially accommodated within the Himalaya [*Lyon-Caen and Molnar*, 1985; *Avouac and Tapponnier*, 1993], where orogen-perpendicular convergence rates vary from 13.3 ± 1.7 mm a^{-1} in the west to 21.2 ± 2.0 mm a^{-1} in the east [*Ader et al.,* 2012; *Stevens and Avouac*, 2015] (Figure 1), and the remainder is distributed farther north. Shortening across the Himalaya is currently accommodated mostly in the Sub-Himalaya, where southward directed thrusting has resulted in the in-sequence development of an extensive fold-and-thrust belt involving the Neogene Siwalik and Quaternary foreland strata [*Powers et al.,* 1998; *Wesnousky et al.,* 1999; *Thakur et al.,* 2007]. An orogen-wide compilation of shortening estimates across the Sub-Himalaya based on balanced and retrodeformed cross sections reveals shortening rates of 3.2 ± 0.7 to 9.7 ± 1.4 mm a^{-1} since the Middle-Upper Siwalik boundary
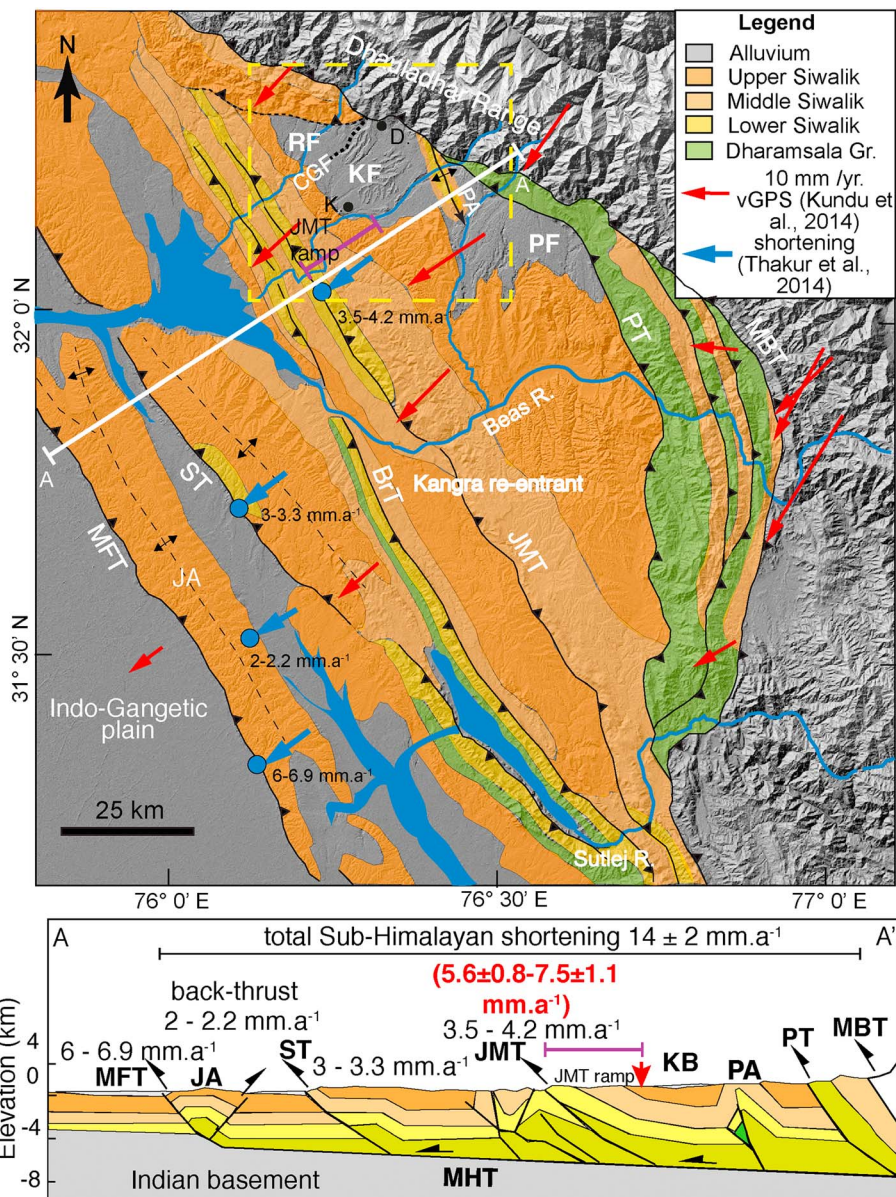
Figure 1. The Himalayan orogen bordering the southern margin of the Tibetan Plateau (inset). Orogen-perpendicular convergence rate (in mm a^{-1}) of the Indian and the Eurasian plate accommodated within the Himalaya [*Stevens and Avouac*, 2015]. Our study area, the Kangra reentrant in the NW Himalaya, highlighted by the blue rectangle, has the lowest amount of present-day convergence.

(Pliocene) [*Hirschmiller et al.*, 2014]. Faulting within the Sub-Himalaya has been mainly accommodated by the Main Frontal Thrust (MFT) since the mid-Pleistocene [*Raiverman et al.*, 1994; *Powers et al.*, 1998; *Wesnousky et al.*, 1999]. For example, studies in central Nepal revealed that the majority of the convergence is accommodated across the MFT, where Holocene shortening rates of ~20 ± 1 mm a^{-1} have been obtained from deformed fluvial terraces [*Lave and Avouac*, 2000], in good agreement with 20 ± 3 mm a^{-1} of shortening from geodetic measurements [*Jouanne et al.*, 2004; *Bettinelli et al.*, 2006; *Stevens and Avouac*, 2015]. *Powers et al.* [1998] proposed a total long-term shortening rate of 14 ± 2 mm a^{-1} in the Kangra reentrant and 11 ± 5 mm a^{-1} in the Dehradun reentrant across the Sub-Himalaya for the Quaternary (1.9–1.6 Ma). In the same region, *Wesnousky et al.* [1999] proposed a minimum shortening rate of 11.9 ± 3.1 mm a^{-1} on the MFT since the Holocene. In the Kangra reentrant, where the GPS-derived slip rate of the MHT has been estimated at 14 ± 1 mm a^{-1} [*Banerjee and Burgmann*, 2002; *Kundu et al.*, 2014], it has been proposed that the bulk of the long-term shortening of 8.5 ± 1.6 mm a^{-1} since 2.7 ± 0.3 Ma [*Hirschmiller et al.*, 2014] has been accommodated along the MFT system [*Thakur et al.*, 2014].

Recently, *Thakur et al.* [2014] proposed that crustal shortening in the Kangra reentrant (Figure 2) is not restricted to the MFT but rather comprises out-of-sequence thrusting partitioned among several subparallel thrusts in the Sub-Himalaya since late Pleistocene time. These thrusts include the Palampur Thrust (PT), the Jwalamukhi Thrust (JMT), the Barsar back thrust (BrT), the Soan Thrust (ST), and other structures (e.g., the Janauri Anticline (JA) on the hanging wall of MFT and its related back thrust) that have grown toward the foreland (Figure 1). *Thakur et al.* [2014] estimated a total shortening rate of 14 ± 2 mm a^{-1} across various structures in the Sub-Himalaya over the last ~30–40 ka (see Figure 2) based on uplifted strath terraces with OSL (Optically stimulated luminescence) dates of the alluvial cover. Because OSL ages based on samples collected in these deposits determine the onset of sediment aggradation rather than the timing of terrace abandonment (the latter of which provides the age of the deformed geomorphic marker), the deformation estimates from *Thakur et al.* [2014] are averaged over longer timescales and hence may underestimate true deformation rates.

In the northwest corner of the Kangra reentrant, the Kangra intermontane basin (Figure 2) stores more than 200 m of late Pleistocene alluvium, which forms a cover on top of tilted Sub-Himalayan strata in the hanging wall of the Jwalamukhi Thrust. This alluvium represents the vestiges of former extensive basin fills that were subsequently reincised [*Sah and Srivastava*, 1992; *Srivastava et al.*, 2009; *Thakur et al.*, 2014; *Dey et al.*, 2016], pointing to a potential feedback between sedimentation-erosion cycles and out-of-sequence faulting. Indeed, sediment removal and an accompanying reduction in lithostatic stress can potentially reactivate structures within an intermontane basin, leading to out-of-sequence deformation [*Burbank and Raynolds*,

Figure 2. Geological map of the Kangra reentrant in NW Sub-Himalaya, showing the major tectonic structures, lithology, and drainages, as well as Pleistocene sediments [after *Steck*, 2003; *Thakur et al.*, 2014]. The yellow dashed rectangle denotes our study area in and around Kangra Basin. GPS motion vectors in the reentrant are plotted after *Kundu et al.* [2014], and shortening rates (blue arrows) are plotted after *Thakur et al.* [2014]. A generalized cross section of the whole Sub-Himalaya along AA' shows the geometry of different structures (modified after *Powers et al.* [1998] and *Thakur et al.* [2014]). Range of shortening rates derived from this study on the Jwalamukhi Thrust (JMT) is shown in bold red text. Abbreviations: MBT: main Boundary Thrust, PT: Palampur Thrust, BrT: Barsar back thrust, ST: Soan Thrust, MFT: Main Frontal Thrust, JA: Janauri Anticline, PA: Paror Anticline, SMA: Surain-Manohargarh Anticline, MHT: Main Himalayan Thrust, CGF: Chambi-Gaj Fault, RF: Rait-Rihlu Fan, KF: Kangra Fan, and PF: Palampur Fan.

1988; *Pavlis et al.*, 1997; *Hilley and Strecker*, 2005; *Pingel et al.*, 2013]. On timescales of 10^4 to 10^6 years, this feedback may be identified and quantified using a combination of sediment archives and landforms, including partially preserved valley fills, alluvial fans, and fluvial terrace systems [*Gibling et al.*, 2005; *Kumar et al.*, 2007]. In this study, we have employed river profile analysis, structural analysis, and cosmogenic radio nuclide (CRN) exposure dating of geomorphic markers (fluvial terraces) in the Kangra reentrant in order to (1) constrain Holocene fluvial incision and terrace formation and (2) to more precisely evaluate the activity of the JMT within the Sub-Himalaya using a fault-bent fold model.

2. Morphotectonic Setting and Stratigraphy of the Kangra Basin

The sinuosity of the MBT and the range front results in segmentation of the range into structural reentrants and salients (Figure 2). Structural reentrants occur where the southward propagation of the deformation front has been less pronounced with respect to neighboring segments. The Kangra reentrant, the largest one, is located in the foothills of Himachal Pradesh, NW India. The Kangra Basin lies in the NW corner of this reentrant, bounded by the MFT to the south and a pronounced topographic front to the north. This topographic front is the hanging wall of the MBT and constitutes the Dhauladhar Range. Elevations of the range decrease systematically until it is truncated by the Ravi River in the west and the Beas River in the east. The sinusoidal nature of the MBT causes the termination of the Kangra reentrant against the Nahan salient on the eastern flank of Beas River (Figure 2).

The Kangra reentrant comprises a nearly 80 km wide section of the Sub-Himalayan fold-and-thrust belt (Figure 2). The Kangra Basin and nearby regions expose deformed sediments dating back to the middle Miocene (~16 Ma) [*Ranga Rao*, 1993; *Brozovic and Burbank*, 2000] (Figure 3). Low-temperature thermochronology indicates that exhumation of the Dhauladhar Range has been ongoing since at least 6–7 Ma [*Deeken et al.*, 2011], thus providing a temporally and spatially well-constrained source for the exposed sediments. These former foreland basin sediments belong to the Siwalik Group, which includes middle Miocene claystone-siltstone (Lower Siwaliks), late Miocene sandstone and silty claystone (Middle Siwaliks), and late Miocene-Pliocene boulder conglomerates (Upper Siwaliks) [*Ranga Rao*, 1993; *Brozovic and Burbank*, 2000]. The Siwaliks are underlain by the early Miocene Dharamsala Group, which is also deformed due to faulting along the JMT and the Palampur Thrust (PT).

An alluvial basin-fill unit of Pleistocene age [*Srivastava et al.*, 2009; *Thakur et al.*, 2014] unconformably overlies all of these strata. The fill constitutes thick, coalesced alluvial fan deposits composed of stream flow and debris flow sedimentary units within the northern sector of the Kangra Basin, but only a thin veneer covering strath terraces within the southern sector, in the hanging wall of the JMT. Limited chronological information based on IRSL (infrared stimulated luminescence) dating of the alluvium suggests that the Kangra Basin started to aggrade prior to 78 ± 18 ka [*Srivastava et al.*, 2009], and thus, a majority of the sedimentary fill accumulated during the last glacial period (~110 to 20 ka) [*Dey et al.*, 2016; *Thakur et al.*, 2014]. Subsequent to the basin filling, regional erosion ensued, and fluvial terraces were sculpted into the previously deposited sediments, resulting in reestablished fluvial connectivity with the foreland [*Srivastava et al.*, 2009].
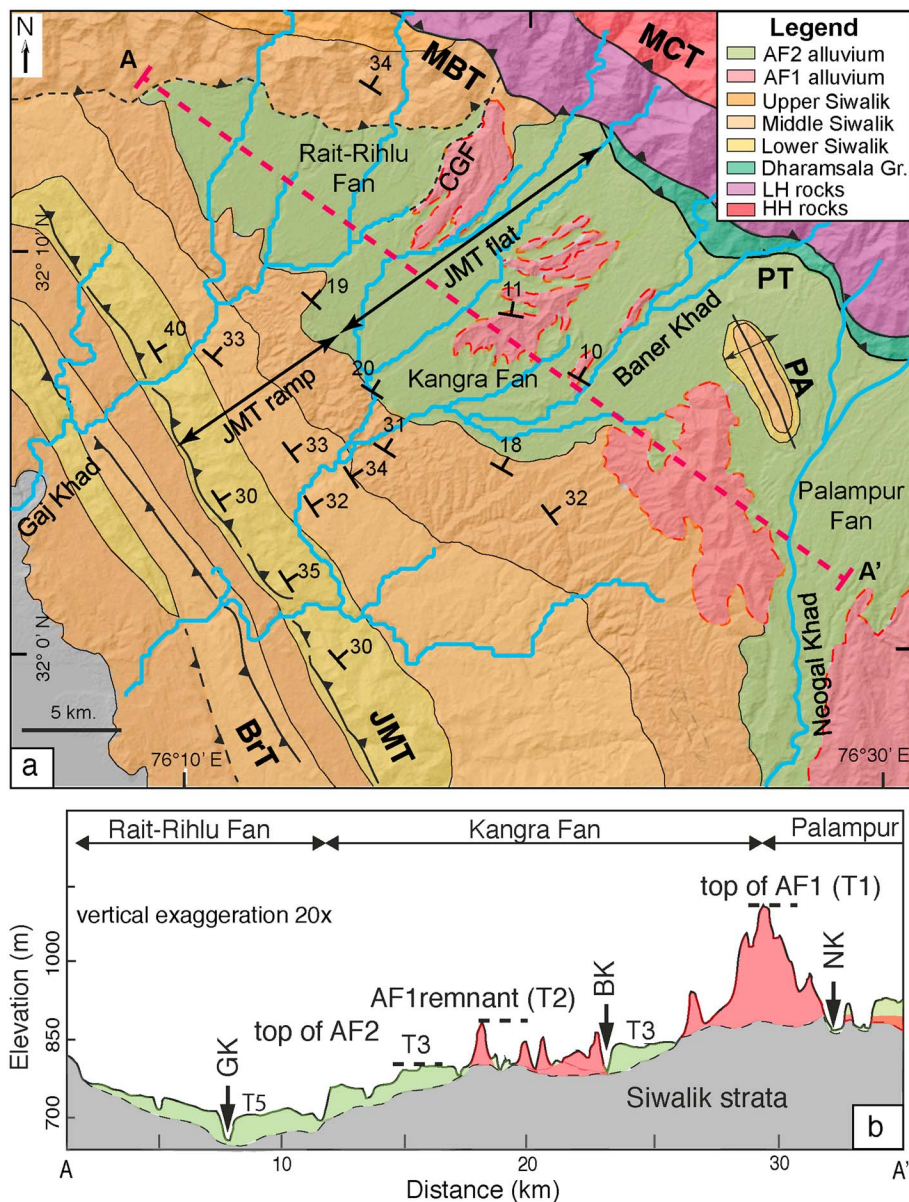
3. Materials and Methods

In this study, we focus on the Rait-Rihlu and Kangra sectors of the Kangra Basin, which are separated by the Chambi-Gaj transfer fault, and drained respectively by the Gaj Khad and the Baner Khad (the local term for river is "Khad") (Figure 3). To characterize the geomorphic features of the area and quantify geomorphic indices potentially indicative of neotectonic deformation, we used on-site field mapping, satellite-derived digital elevation model (DEM) analysis, and cosmogenic-nuclide surface-exposure dating of fluvial terraces. For our geomorphic analyses, we used Cartosat-1, 1 arc sec elevation data (http://bhuvan.nrsc.gov.in/data/download/index.php), which we resampled to 30 m resolution. All DEM-related analyses were performed using ArcGIS and/or MATLAB.

3.1. Terrace Mapping and Profile Analysis

We delineated fluvial terraces within the Baner Khad and Gaj Khad watersheds both in the field and with the help of DEM analysis to determine their regional extent. We used two different approaches to identify terraces from the DEM. First, to map the spatial extent of different terrace levels, we calculated a slope map from the DEM and identified pixels with slope values of <4° as terraces. In addition, to map the location and heights of the terraces along longitudinal stream profiles, we used functions from TopoToolbox 2.0 [*Schwanghart and Scherler*, 2014] to extract longitudinal river profiles and hillslope gradients within a 1 km wide swath on either side of the thalweg. Thus, a terrace preserved along the river plots as a cluster of near-zero hillslope values above the stream profile on a linear plot of elevation versus stream length.

In the field, we validated our DEM-based mapping and verified locations, extents, and elevations of premapped terraces using handheld GPS measurements. To constrain absolute terrace heights, we averaged multiple elevation measurements from the GPS and the DEM. The average of the GPS elevation data from

Figure 3. (a) Geological map of the study area within Kangra Basin showing major tectonic boundaries and rock types along with structural measurements and mapped alluvial fan sequences. Different sectors of the basin and the two alluvial fan remnants (AF1 and AF2) are shown. The line AA' represents transect shown in the inset. (b) Schematic cross section of Kangra Basin, drawn parallel to the mountain front showing the two fan remnants and modern drainage. Abbreviations: LH: Lesser Himalaya and HH: Higher Himalaya.

each terrace was used to define the mean terrace elevation, whereas the range of elevation values defines the uncertainty. In addition to the terrace profiles, we extracted the maximum, mean, and minimum elevations within a 2 km wide swath along the major river channels from the DEM.

Following our mapping of different terrace levels, we determined the volume of sediment that has been removed since deposition of the first alluvial fan deposits in the Kangra Basin. The volume was calculated using the ArcGIS 10.1 3-D analysis toolbox and by creating a virtual TIN (triangular irregular network) with the same mean slope as the top of the older fill. The intersection of that virtual TIN surface with the DEM basin boundary yielded a cut-fill volume estimate, the accuracy of which depends on the resolution of the DEM and process iterations while creating the TIN. The cut-and-fill volume represents the net sediment removed from the basin since the time of maximum basin fill (~50 ka) [Dey et al., 2016].

3.2. Stream Profiles

Global observations across a broad spectrum of tectonic and climatic regimes have revealed a power law scaling between the local river gradient and upstream contributing area:

$$S = k_s A^{-\theta} \tag{1}$$

where S is the stream gradient (m/m), k_s is the steepness index ($m^{2\theta}$), A is the upstream drainage area (m^2), and θ is the concavity index [*Flint*, 1974; *Whipple and Tucker*, 1999]. Normalized steepness index values (k_{sn}) are steepness indices calculated using a reference concavity value (θ_{ref}), which is useful when comparing steepness index values from different river systems [*Wobus et al.*, 2006]. Following an increase in rock uplift rate, a stream will tend to readjust in a way that will enable faster incision, which typically includes a steepening of its bed and a reduction of its width (assuming constant runoff). As a consequence, the channel gradient will increase first in the downstream reaches of the higher uplift zone and migrate upward. The upstream end of this steepened section is marked by a "knickpoint" on the river long profile that separates adjusted, steeper (high k_{sn}) reaches from unadjusted, "relict" (lower k_{sn}) reaches [*Whipple and Tucker*, 1999]. Tectonically generated knickpoints migrate upstream with time [*Whipple and Tucker*, 1999; *Snyder et al.*, 2000], until, at topographic steady state, areas of higher rock uplift will be characterized by higher k_{sn} values. In the case of a thrust fault, where spatially variable rock uplift rates result from the increasing dip angle of the thrust plane from the gentle-sloping flat to the steeper ramp, we expect quasistatic knickpoints that separate zones of higher uplift and lower uplift (higher and lower k_{sn} values) [*Wobus et al.*, 2006].

Because river incision through more resistant rocks requires greater stream power compared to less resistant rocks, knickpoints may also be observed near the contact between harder and weaker units, with higher k_{sn} values in areas underlain by harder units [*Miller*, 1991; *Duvall et al.*, 2004]. These knickpoints are generally anchored to the lithologic contacts [*Duvall et al.*, 2004], which helps to distinguish them from transient (tectonically generated) knickpoints and potentially also from quasistatic knickpoints separating zones of differing uplift rates.

We extracted stream profiles from the DEM using the MATLAB-supported stream profiler tool (www.geomorphtools.org) following the procedure of *Wobus et al.* [2006]. We performed automated k_{sn} extraction using a critical area of 10^6 m^2 to assign channel heads, a smoothing window of 500 m, and a θ_{ref} value of 0.45.

3.3. Valley-Floor Width to Valley-Height Ratio

The valley-floor width to valley-height ratio is used as a proxy for rock uplift or incision [*Bull*, 2008]. We calculated valley-floor width to valley-height ratios (Vfw:Vh) using the following equation:

$$Vfw : Vh = 2Vfw/[(E_{ld} - E_{sc}) + (E_{rd} - E_{sc})] \tag{2}$$

where Vfw is the valley-floor width, Vh is the valley-height, E_{ld} is the elevation of the river-left valley divide, E_{rd} is the elevation of river-right valley divide, and E_{sc} is the elevation of the thalweg (all in the same length scale) [*Bull*, 2008]. A higher valley-floor width to valley-height ratio is typically associated with lower incision or uplift rates, whereas rapid uplift causes enhanced vertical incision, leading to a V- or I-shaped channel geometry and a lower Vfw:Vh ratio [*Pinter and Keller*, 1995; *Bull*, 2008]. We determined the Vfw:Vh ratios of the axial rivers, measured at 400 m intervals along the thalweg. For this measurement, we used the Globalmapper tool on 30 m resolution Cartosat-1 data.

3.4. Surface-Exposure Dating Using In Situ [10]Be

We determined surface-exposure ages of the preserved terraces using concentrations of the in situ cosmogenic radionuclide Beryllium-10 ([10]Be) from amalgamated pebble samples collected from depth profiles and terrace surfaces, following approaches applied in numerous settings [e.g., *Repka et al.*, 1997; *Brocard et al.*, 2003; *Schaller et al.*, 2009; *Schildgen et al.*, 2012]. A description of the general approach can be found in the supporting information. For depth profiles, we excavated a 2.2 to 2.5 m deep pit in every location and collected samples at roughly 30 cm depth intervals, including the surface sample, which represents the top 0–10 cm of the profile. We sampled >20–30 granite and quartzite pebbles (2–3 cm diameter) per depth interval. For the surface-only samples, we sampled clasts of similar size from all over the surface (apart from the terrace edges) and from up to 10 cm depth. The absence of gullies on the terrace surfaces and any remnants of thicker soils suggests that if surface erosion has occurred, it has likely been minimal. However,

some of the flat terrace surfaces have been used for agriculture for many decades, implying that at least some of our samples will have been affected by erosion and/or mixing of the soil.

Samples were processed at the University of Potsdam, the GFZ Potsdam, and the University of California, Santa Barbara. Samples were crushed and ground to 250–500 μm grain size, then magnetically separated and etched with HCl and multiple iterations of 1% HF before further chemical processing. After a final leach in aqua regia, each sample was dissolved in concentrated HF. Subsequently, 150 μg of ^{9}Be carrier was added to each sample. The sample matrix was removed by column chemistry. Ultimately, pure Be(OH)$_2$ precipitate was obtained and oxidized to BeO. The 100 μg of Nb powder was admixed with each sample. The targets were pressed and packed for accelerator mass spectrometer (AMS) measurements at Lawrence Livermore National laboratory (relative to 07KNSTD3110 as standard) and the University of Cologne (KN01-6-2 and KN01-5-3 as standards) [*Dewald et al.*, 2013]. Process blanks with a ^{10}Be/^{9}Be ratio of 2.2×10^{-16} (for samples measured at the Cologne AMS) and 2.0×10^{-16} (for samples measured at the Lawrence Livermore AMS), respectively, were subtracted from the measured sample ratios.

All exposure ages reported in this study are based on the time-dependent production rate scaling scheme by *Lal* [1991] as updated by *Stone* [2000], provided in the CRONUS Earth web calculator version 2.0 (http://web1. ittc.ku.edu:8888/2.0/; *Marrero et al.* [2016]). We refer to this scaling framework as "Lm" [*Balco et al.*, 2008] in the following. Topographic shielding of production rates is based on *Dunne et al.* [1999] and was calculated based on field measurements with a geological compass and the tool provided by *Hidy et al.* [2010]. To determine surface-exposure ages corrected for nuclide inheritance and surface erosion from the depth profiles, we performed Monte Carlo simulations (1,000,000 iterations) using the simulator provided in *Hidy et al.* [2010]. The nuclide inheritance of each sample determined from depth profiles is assumed to be similar, if the pit represents a single fill. That value is subtracted from the surface concentration prior to calculating an exposure age. The simulation was done assuming a reference sea level high latitude (SLHL) total ^{10}Be production rate of 4.00 atoms g^{-1} a^{-1} [*Borchers et al.*, 2016], a density of 1.9 to 2.1 g cm^{-3}, an attenuation length of 160 ± 5 g cm^{-2} for neutron spallation [*Dunne et al.*, 1999], an erosion rate of 0 to 0.2 cm ka^{-1}, and a total erosion threshold of 0 to 20 cm. Using a higher erosion threshold results in older ages, but as mentioned above, we saw minimal direct evidence of erosion on the very flat terraces. Also, the tight clustering of our ages from individual terraces argues for minimal erosion. Exposure ages from the depth profiles were first obtained with the Monte Carlo simulator [*Hidy et al.*, 2010] based on the time-independent surface production scaling scheme by *Lal* [1991] and *Stone* [2000]. The resulting ages were then recalculated for time-dependent production rates using the CRONUS-Earth web calculator version 2.0.

For locations in which we only collected surface samples, we assume that the samples represent a mixture of 0–10 cm depth from the surface due to bioturbation and anthropogenic overprint of the terrace surface; hence, we applied a shielding factor equivalent to 5 cm depth on the surface production rate to calculate the ages. An inheritance correction was applied for each of the surface-only samples, which entails subtracting the inherited concentration from the surface concentration. Specifically, the ^{10}Be concentration that accumulated since exposure was determined by subtracting the inheritance derived from depth profiles (from depth profiles of the same terrace level) from the measured concentration of the surface sample (Table 2). For terrace level T3, we used the average of the two inheritance values (from pits T3-P1 and T3-P2) as the model inheritance. For T4, the inheritance of T3 was used, and for T6, the inheritance from T5 (T5-P1) was used. These inheritance-corrected concentrations were used to determine the Lm ages with the CRONUS web calculator.

3.5. Constraining Deformation Across the Jwalamukhi Thrust (JMT)

We used the recorded offset in the heights of terrace level T3 along Baner Khad across the JMT to constrain the fault displacement since the time of terrace formation. To calculate this offset, we determined terrace heights along a profile line perpendicular to the JMT. We performed two independent estimates of the terrace offset. In the first approach, we used the hillslope-angle plot using the 30 m resolution DEM (vertical accuracy defined by the relative mean standard error, RMSE, of 3.6 to 4.4 m) along the Baner Khad, where the lower envelope of the hillslope angles <4° was used to identify terrace pixels and a best fit line through the terraces was then extrapolated to a vertical plane that passes through the JMT. For this analysis, we chose terraces alongside the stream segments that flow perpendicular to the strike of the fault. In a second approach, we used multiple point-averaged elevation data from handheld GPS measurements in the field

to identify the terrace level and quantify its height in multiple locations. We fit linear trends through our GPS measurements from the T3 terrace level on both sides of the fault and projected those trends onto a N50°E azimuth profile line (perpendicular to the strike of JMT), in an approach analogous to that of *Thompson et al*. [2002]. The difference between the DEM elevations and the multiple point-averaged, GPS-derived ground-control points is ±3 m on average.

In both cases, the elevation difference of the extrapolated terrace level on the vertical plane passing through the JMT denotes the terrace offset (dz). To determine the terrace offset and estimate its error, the following equation was used:

$$dz = (a - b) \pm \sqrt{da^2 + db^2} \qquad (3)$$

where a is the intercept of the best fit line on the hanging wall with the fault plane, b is the intercept of the best fit line on the footwall with the fault plane, da is the uncertainty in the fit on the hanging wall, and db is the uncertainty in the fit on the footwall.

Subsequently, based on an assumed fault-bend fold geometry, which has been widely proposed in studies of Sub-Himalayan deformation [*Lave and Avouac,* 2000; *Mugnier et al*., 2004; *Mukhopadhyay and Mishra*, 1999], we converted the vertical component of the total slip across the JMT into fault displacement and crustal shortening rates.

4. Field Observations and Results

4.1. Sediment Architecture

Within the Pleistocene alluvial fill of the Kangra Basin [*Sah and Srivastava*, 1992; *Srivastava et al*., 2009] at least two generations of alluvial fans have been recognized, which reflect at least two sediment aggradation phases. We name these alluvial fills AF1 and AF2 according to their stratigraphic order (Figure 3). The coarser fraction of the fills constitutes primarily well-rounded, poorly sorted, clast-supported, polished pebbles and boulders of alluvial origin (Figures 4b, 4d, and 4e), although occasional layers of subangular, matrix-supported, unsorted boulders record the input of debris flows. In addition, there are isolated layers of highly angular granite clasts that are underlain by heavily cataclasized fragments, which we interpret as landslide deposits [e.g., *Shreve*, 1968].
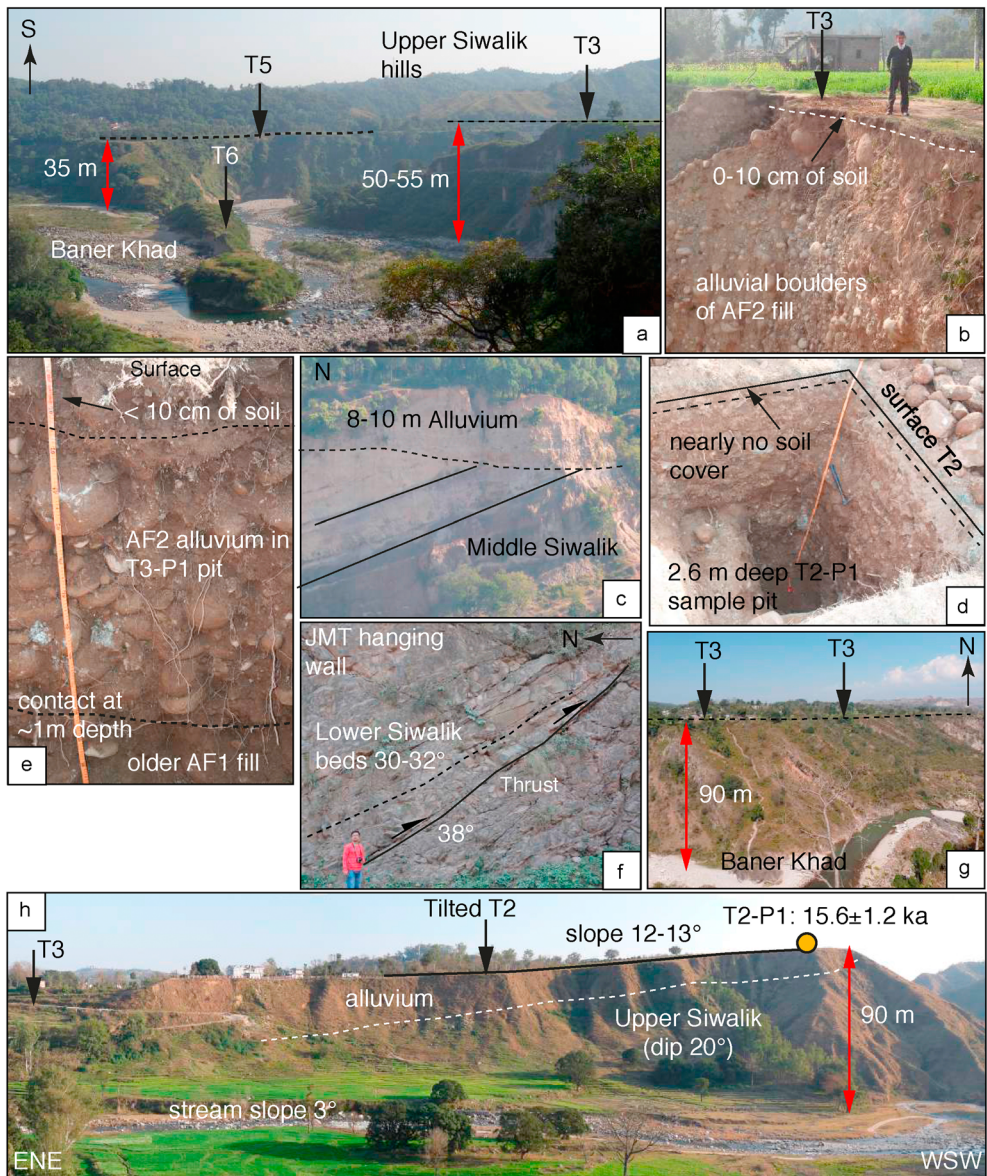
The older alluvial fan (AF1) has a thickness of up to > 200 m but is only represented by a few surface remnants in the eastern sector of the Baner Khad watershed, south of the Paror anticline (Figure 3). These remnants can be observed as small hillocks in the center of the Kangra Basin and east of the Chambi-Gaj Fault, south of the town of Dharamsala (Figure 3). The tops of these AF1 remnants at the center of the basin, where the fill thickness is 120 to 140 m, are occasionally flat and have been considered as the highest preserved surface relics [*Dey et al*., 2016]. The AF1 alluvial fill is late Pleistocene in age, ranging from 78 ± 18 to 17 ± 2 ka based on IRSL data [*Srivastava et al*., 2009], whereas the highest preserved surfaces have cosmogenic [10]Be-based exposure ages of 59 ± 5 ka to 46 ± 6 ka [*Dey et al*., 2016]. The younger fan deposit, AF2, is better preserved and is extensively exposed throughout the basin, with the top of the fill located 55 to 60 m above the river bed. Based on our DEM analyses, we estimate that only 10 to 15% of the original late Pleistocene alluvial fill remains within the basin.

The contact between the fill units and the underlying Siwalik strata is mostly a pronounced angular unconformity (Figure 4c). The thick AF1 conglomerates may point toward damming or severed drainage conditions in the hanging wall of the JMT; alternatively, they might reflect a fluvial system that was overwhelmed by a massive influx of sediments prior to ~78 ka [*Srivastava et al*., 2009].

4.2. Fluvial Terraces

4.2.1. Fluvial Terrace Levels
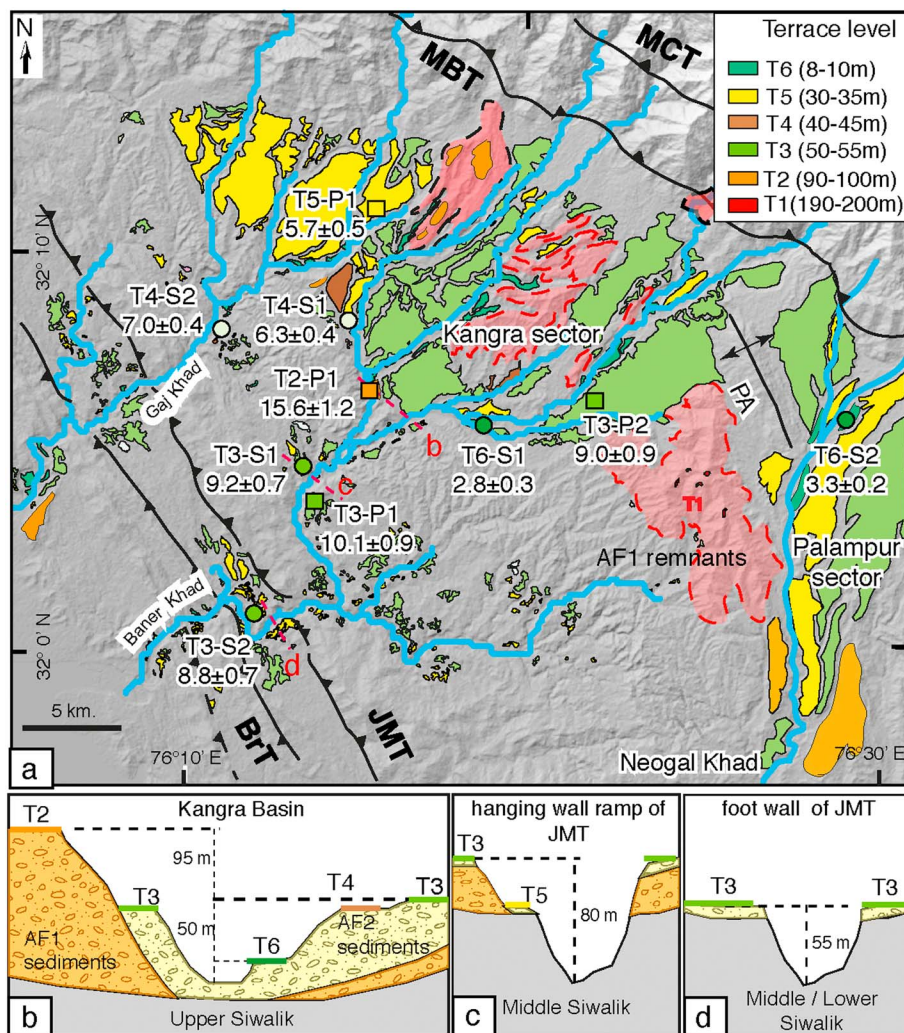
Fluvial terraces in the northwest corner of the Kangra reentrant comprise fill (Figures 4a and 4b), strath, and cut-and-fill terraces (Figures 4c and 4g). We observed only fill terraces within the Kangra Basin, where the streams are mostly still incising the Pleistocene alluvium. In contrast, south of the basin, we observed both strath and cut-and-fill terraces. The cut-and-fill terraces comprise 5 to 20 m of alluvium atop a strath terrace carved into tilted Siwalik units over the ramp of the JMT (Figure 2, inset), whereas strath terraces comprise a

Figure 4. Field photos from the Kangra reentrant. (a) Different terrace levels sculpted into the AF2-alluvium covering the tilted Upper Siwaliks, south of Kangra town along the Baner Khad. (b) View of the stratigraphy of alluvial fill within Kangra Basin and T3 surface from the top. Note that most terrace tops are only covered by a thin soil layer (with few well-rounded quartz clast ⌀ ~ 2–3 cm) of ~10 cm. (c) Angular unconformity between northeasterly tilted (30°–35°) Middle Siwalik beds and overlying alluvium. (d) T2-P1 pit for cosmogenic radio nuclide (CRN) depth profile sampling. (e) T3-P1 pit for CRN depth profile sampling, again showing a very thin soil layer on top, followed by a nearly 1 m thick AF2 conglomeratic layer and more strongly weathered AF1 conglomerates below. (f) Brittle fault zones (dip 38°) in the vicinity of the JMT and the bedding planes (dip 30–32°) of Lower Siwalik units, near the bridge on Baner Khad, near Ranital. (g) Thin alluvial fill (1–2 m thick) with T3 terrace surface above strath terrace and over the tilted Middle Siwalik beds (hanging wall of JMT). (h) View of north-north-easterly back-tilted terrace T2, to the west of Kangra town, seen from neighboring T3 surface. Slope of the surface and slope of the stream are 12–13°NE and 3°SW, respectively. All together, 15°–16° of back tilt of the terrace top surface has occurred since formation. CRN depth profile T2-P1 (see Figure 6a) has been sampled at the top of this terrace—see orange dot for approximate location.

veneer of less than 1 m of conglomeratic fill over a bedrock strath (Figure 4g). These observations are consistent with the terrace descriptions by *Thakur et al.* [2014].

As described in *Dey et al.* [2016], we identified at least six terrace levels within the basin and named these T1 through T6, in order of decreasing elevation above the thalweg (Figure 5a). We attribute the highest flat

Figure 5. (a) Map of fluvial terraces in Kangra region with cosmogenic radio nuclide (CRN) sampling sites and respective exposure ages. (b–d) Three cross sections are drawn to show how the terrace heights and terrace types vary along the river channel. Within the basin in Figure 5b, the terraces are thick fill terraces, whereas in Figures 5c and 5d, due to rock uplift in vicinity of the JMT-ramp, the rivers are incising into bedrock (here Siwalik units), forming strath terraces with thin alluvial veneers (Figure 4g) and deeply incised narrow canyons.

terrace levels associated with well-rounded fluvial boulders (relicts of the AF1 fill) to the T1 terrace level. T1 is nearly 200 m above the nearest riverbed. Below T1, terrace level T2 is sculpted into the AF1 fan remnants. The height of T2 varies from 90 to 110 m above the present-day thalweg (Figure 5b). Incision following the AF2 aggradation generated levels T3 (45 to 55 m above the thalweg), T4 (35 to 40 m), T5 (30 to 35 m), and T6 (10 m) (Figure 5b). These different terrace levels reveal important information concerning variations in climate and sediment flux in the region [*Dey et al.*, 2016], but for this contribution, we solely focus on the best preserved terrace level (T3) as a strain marker that helps us evaluate the degree of Holocene tectonic activity in the Kangra reentrant.

The heights of terrace level T3 above the modern thalweg vary along the course of the Baner Khad. Near the center of the basin, the height of T3 above the thalweg ranges between 42 and 50 m, then gradually increases to ~100 m near the JMT, and after crossing JMT, the height drops again to 50–55 m (Figures 5b–5d). Furthermore, a terrace remnant related to level T2 is preserved at the southern extremity of the basin and is back tilted by 12 to 13° toward the NE. The clasts within the fill are oriented subparallel to the surface, showing an angular unconformity with the underlying Siwalik units, which dip more steeply (20 to 22°) to the NE (Figure 4h).

Table 1. Sample Details With ^{10}Be Concentrations and Measured Uncertainties

Terrace ID	Sample Names	Depth or Depth Interval (cm)	^{10}Be (atoms g^{-1})	^{10}Be Uncertainty (atoms g^{-1})	Surface Production Rate (atoms g^{-1} a^{-1})	Topographic Shielding	Inheritance From Depth Profiles (10^3 atoms g^{-1})[b]	Modeled Surface Concentration (10^3 atoms g^{-1})[c]	Inheritance-Corrected Surface Concentration (10^3 atoms g^{-1})[d]
T2-P1	T36[a]	0–5	112494	3118	6.16	0.99	8.50 ± 0.50	104.76 ± 6.50	96.26 ± 6.52
	T03	10	92184	3070					
	T35[a]	30	68778	2011					
	S21	60	44591	2256					
	T30[a]	90	29742	990					
	T02	120	23518	1050					
	T01	200–205	21064	1490					
	T32[a]	250	32396	818					
T3-P1	T27	5	57496	2153	5.59	0.99	5.20 ± 0.30	61.81 ± 4.50	56.61 ± 4.51
	T06	30	50184	1864					
	T26	60–65	26537	1091					
	T05	90	24527	1176					
	T04	115–120	49890	1720					
	T31[a]	130–135	41478	1564					
	T28	210–215	12708	702					
	T34[a]	250–255	6332	554					
T3-P2	T11	15	49264	2050	6.09	0.98	5.30 ± 0.40	60.93 ± 5.20	55.63 ± 5.22
	S17	30	36595	1746					
	T14	60	35174	1536					
	S18	90	25973	1462					
	S19	150	11960	762					
	S20	230	6597	544					
T3-S1	S11	0–10	54576	3409	5.58	0.97	5.30 ± 0.40	58.06 ± 3.41	52.76 ± 3.43
T3-S2	S22	0–10	46213	2649	5.13	0.98	5.30 ± 0.40	49.16 ± 2.65	43.86 ± 2.68
T4-S1	T09	0–10	40296	1872	5.93	0.98	5.30 ± 0.40	42.87 ± 1.87	37.57 ± 1.91
T4-S2	T08	0–10	42693	1925	5.51	0.96	5.30 ± 0.40	45.42 ± 1.93	40.12 ± 1.97
T5-P1	T12	10–15	32673	1637	6.27	0.98	6.00 ± 0.40	41.90 ± 3.01	35.90 ± 3.03
	S4	30	26105	1989					
	S5	50	24224	1909					
	T13	75–80	20931	1167					
	S6	150	7118	626					
T6-S1	S12	0–10	19774	1366	5.81	0.98	6.00 ± 0.40	21.04 ± 1.37	15.04 ± 1.43
T6-S2	T10	0–10	29269	1515	7.71	0.97	6.00 ± 0.40	31.13 ± 1.52	25.13 ± 1.57

[a]Samples processed at UCSB and measured at Lawrence Livermore National Laboratory, USA. AMS standard: 07KNSTD3110 (2.85×10^{-12}). Process blank ^{10}Be/^{9}Be: 2.0×10^{-16}. Remaining samples are processed in GFZ Potsdam and measured at CologneAMS, Germany. AMS standard: KN01-6-2 (5.35×10^{-13}) and KN01-5-3 (6.32×10^{-12}), Process blank ^{10}Be/^{9}Be: 2.2×10^{-16}. Blank ratios were subtracted from measured ratios.
[b]Inheritance obtained from ^{10}Be depth profiles [*Hidy et al.*, 2010]. For level T3 and T4, average of the two inheritance values (from T3-P1 and T3-P2) is used as model inheritance. For T5 and T6, the inheritance from T5-P1 is used.
[c]Model surface concentration means either depth-corrected concentration from surface-only samples or Monte Carlo simulation–derived surface concentration for depth profile samples.
[d]Inheritance corrected ^{10}Be concentration = model surface concentration − inheritance. Density: 1.9–2.1 g cm^{-3}.

Table 2. Surface-Exposure Ages (According To Lm Scaling Framework [*Balco et al.*, 2008]) of the [10]Be Samples From T2-T6 Terraces Along With the Sample Locations

Terrace ID	Latitude (deg)	Longitude (deg)	Elevation (m)	Inheritance-Corrected Surface [10]Be Concentration $(10^3$ atoms g$^{-1})^a$	Mean Surface-Exposure Age With External Uncertainty (Lm Age) (ka)[b,c]
T2-P1	32.10649	76.26223	750	96.26 ± 6.52	15.6 ± 1.2
T3-P1	32.05772	76.22650	625	56.61 ± 4.51	10.1 ± 0.9
T3-P2	32.09825	76.34386	750	55.63 ± 5.22	9.0 ± 0.9
T3-S1	32.07733	76.22884	650	52.76 ± 3.43	9.2 ± 0.7
T3-S2	32.01226	76.21296	530	43.86 ± 2.68	8.8 ± 0.7
T4-S1	32.11710	76.26030	715	37.57 ± 1.91	6.3 ± 0.4
T4-S2	32.13490	76.18970	632	40.12 ± 1.97	7.0 ± 0.4
T5-P1	32.18295	76.27620	785	35.90 ± 3.03	5.7 ± 0.5
T6-S1	32.09243	76.33201	690	15.04 ± 1.43	2.8 ± 0.3
T6-S2	32.08780	76.49418	1082	25.13 ± 1.57	3.3 ± 0.2

[a]Inheritance-corrected [10]Be concentrations calculated in Table 1.
[b]Lm ages refer to time-dependent *Lal* [1991] and *Stone* [2000] production model.
[c]Lm ages calculated using SLHL reference production rate of 4.00 atoms g^{-1} a^{-1} [*Borchers et al.*, 2016] in CRONUScalc web calculator [*Marrero et al.*, 2016].
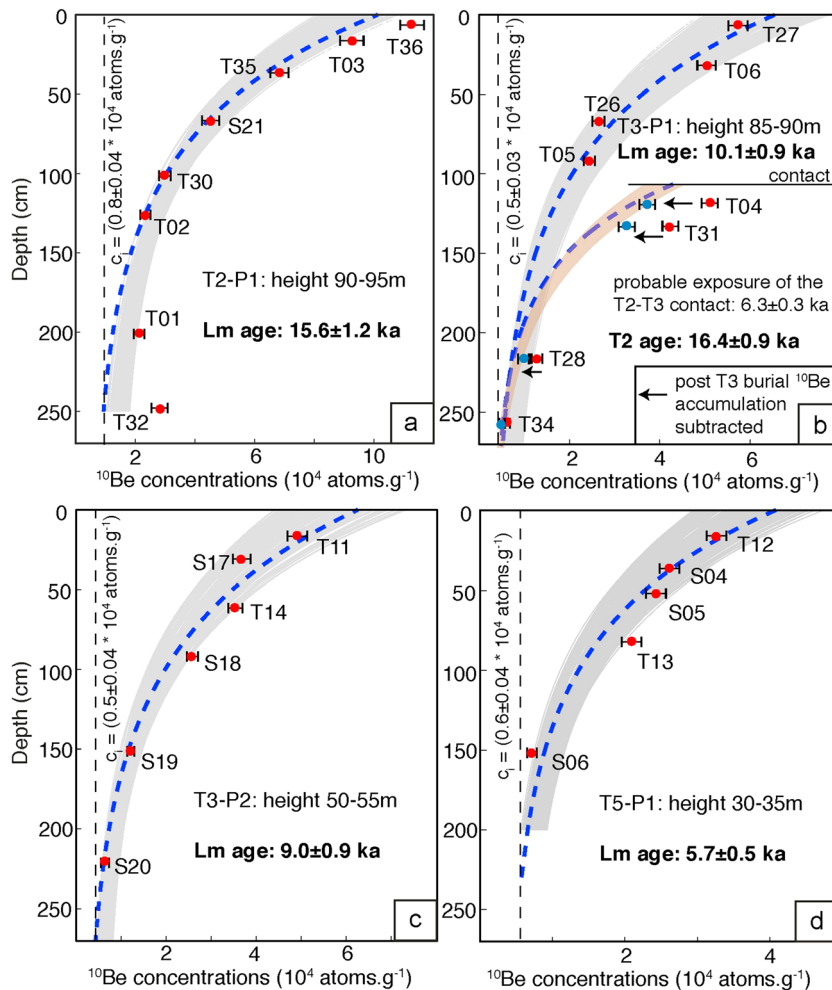
4.2.2. Terrace-Exposure Ages and Published OSL Ages

In situ [10]Be surface-exposure ages of the sampled terraces (Figure 5a) are in agreement with our field observations, revealing successively younger ages with decreasing height above the thalweg. Details of sample locations, depths beneath the terrace surface, [10]Be concentrations, surface production rates, topographic shielding factors, and model-derived surface concentrations are listed in Table 1; terrace-exposure ages and their locations are in Table 2. Surface-exposure ages from terrace level T1 (two sublevels) and T2 (higher sublevel) are reported in *Dey et al.* [2016].

For the single depth profile from terrace level T2 (T2-P1) (Figure 6a), we obtain a well-constrained exposure age of 15.6 ± 1.2 ka (Table 1). One depth profile from terrace level T3, located close to the village of Jalari (T3-P1) (Figure 4e), reveals a more complex pattern of [10]Be concentrations. This pattern may reflect two alluvial fill units interrupted by a period of exposure, as the data appear to define two trends of exponentially decreasing concentrations with depth: an upper trend between the surface and ~100 cm depth, and a lower trend starting between 100 and 120 cm depth and continuing to the bottom of the pit (Figure 6b). However, we did not observe any substantial change in the clast compositions with depth nor did we recognize any depositional hiatus or soil layer separating the two trends in the samples. The only visible difference was in the clast roundness and the degree of weathering: the upper 1 m of the pit was rich in polished and stronger clasts compared to the lower part of the pit, suggesting the occurrence of a later aggradation event potentially related to a lateral shift of the braided fluvial network, as we observed commonly in the modern river network of the study area. Depth profile simulations of the upper fill unit (upper exponential trend comprising the top four samples) furnish a surface-exposure age of 10.1 ± 0.9 ka (Table 2 and Figure 6b). To simulate the exposure time of the bottom-fill unit, the concentrations of the four bottom samples were first corrected for postburial production using the concentration curve derived from the upper fill unit (we subtracted the postburial nuclide accumulation from the measured concentrations of the bottom-fill unit). Following this correction, the depth profile simulations of the lower fill suggest that the inferred contact between the two fills was exposed for 6.3 ± 0.3 kyr before the upper fill covered it (Figure 6b). Interestingly, the absolute exposure age for the proposed contact (16.4 ± 0.9 ka, based on adding the exposure age of the upper unit to the exposure duration of the lower unit and instantaneous deposition of the upper fill unit) is in good agreement with the T2-P1 exposure age (15.6 ± 1.2 ka). The second depth profile in terrace level T3 (T3-P2) yields a surface-exposure age of 9.0 ± 1.0 ka (Figure 6c and Table 2). The single depth profile from terrace level T5 (T5-P1) yields an age of 5.7 ± 0.5 ka (Figure 6d).

Surface samples from terrace level T3, samples T3-S1 and T3-S2, yield exposure ages of 9.2 ± 0.7 ka and 8.8 ± 0.7 ka, respectively. Two surface samples from terrace level T4, T4-S1 and T4-S2, provide exposure ages of 6.3 ± 0.4 ka and 7.1 ± 0.4 ka, respectively. Two more surface samples from the youngest terrace level (T6), T6-S1 and T6-S2, yielded exposure ages of 2.8 ± 0.3 ka and 3.4 ± 0.2 ka, respectively (Table 2).

In comparison, *Thakur et al.* [2014] reported OSL ages of the alluvium overlying the Siwalik strath terraces and proposed aggradation phases at ~32 to ~30 ka, ~23 to ~19 ka (both phases considered part of the AF1 fill in

Figure 6. ^{10}Be concentrations and exposure ages inferred from Monte Carlo simulations of depth profiles, where C_i is the model-derived inheritance and red circles represent the samples from specific depth horizons (see Table 1 for details). (a) Depth profile of T2-P1, sampled from the tilted terrace level T2 (see Figures 4g and 4h). (b) Depth profile of T3-P1, sampled from terrace level T3 along the Baner Khad. Our favored interpretation is that it comprises two different fill events resulting in two decreasing trends (red dashed lines) of ^{10}Be with depth. Due to two-stage filling of the sediments sampled, the concentrations of the samples from the lower unit were corrected for production after the subsequent burial. The blue circles represent the sample concentrations corrected for preburial ^{10}Be accumulation. (c) Depth profile of T3-P2 sampled from terrace level T3 along the Baner Khad. (d) Depth profile of T5-P1 sampled from terrace level T5 along Gaj Khad.

this study), and ~14 to ~11 ka (AF2 fill). Our ^{10}Be exposure ages from the terraces (terrace level T2 sculpted into AF1 remnants and levels T3-T6 sculpted into AF2 fill) postdate the OSL ages that underlie them. Hence, our results are stratigraphically and chronologically consistent with OSL-derived ages of the fill.

4.3. Shortening Rate on the JMT

As described in section 4.2.1, we relate the change in the height of terrace level T3 across the JMT to recent fault displacement since the time of terrace abandonment, providing us with a time-averaged uplift rate on the JMT-ramp. To calculate the shortening or slip rate, accurate knowledge of the dip of the fault plane is crucial. In the field, we measured the dip of several fault zones close to the trace of the JMT in the vicinity of the Baner Khad (Figure 4f). We obtained a mean dip of 38° for fault planes cutting the Siwalik bedding, which dips at a slightly lower angle of 32–35° toward the NE. Both *Powers et al.* [1998] and *Prasad et al.* [2011] assumed an average dip of 30° for the JMT from seismic reflection profiles at a depth of 2–6 km for a section running parallel to, but ~15–20 km to the east of our study area. Hence, we calculate shortening rates based on three different possible thrust fault-dip angles: the average dip measured in the field (38°), the dip from seismic

Table 3. Estimation of Uplift, Shortening, and Slip Rates Across the JMT Based for Varying Fault-Dip Angles

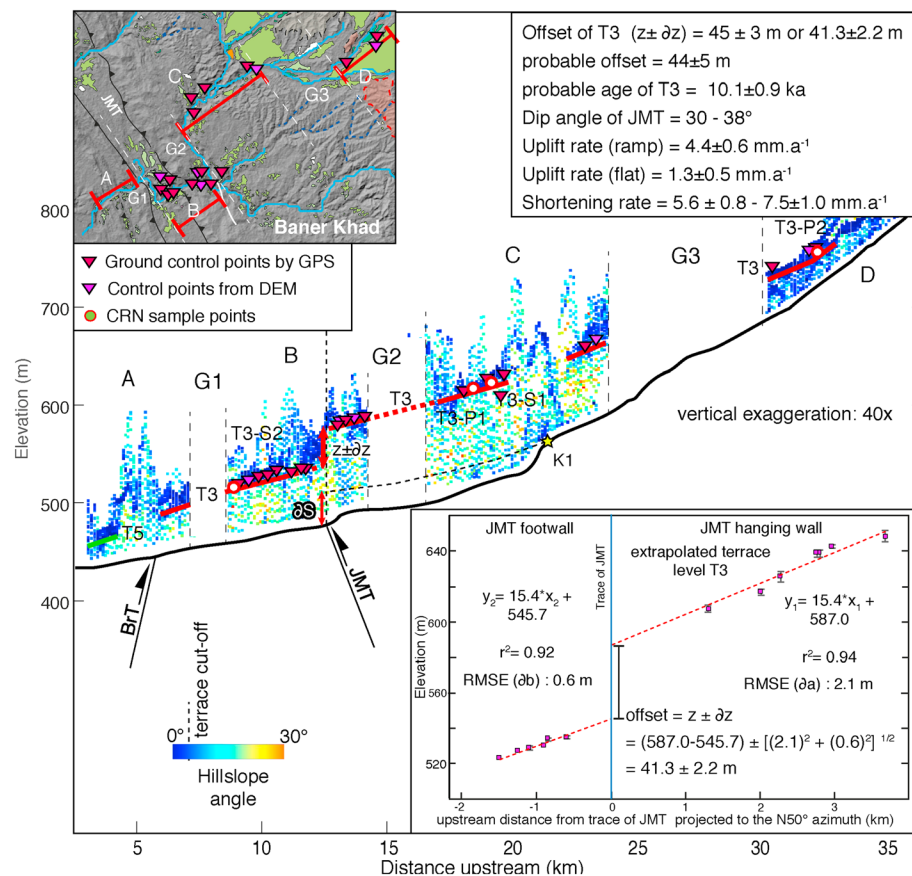| Offset of T3 (m)[a]	Age of T3 (ka)	Thrust Dip (deg)	Uplift Rate on Ramp (mm a^{-1})	Shortening Rate (mm a^{-1})	Slip Rate (mm a^{-1})
44 ± 5	10.1 ± 0.9	30	4.4 ± 0.6	7.5 ± 1.1	8.7 ± 1.2
		34		6.4 ± 0.9	7.8 ± 1.1
		38		5.6 ± 0.8	7.0 ± 1.0

[a]Offset of T3 is estimated by two independent measurements from the DEM and the handheld GPS. The difference between these measurements was propagated as uncertainty on the offset value.

reflection profile (30°), and a mean of these two dips (34°). In Table 3, we report the resulting range of fault slip (FS) and shortening rate (S) estimates based on the following equations:

$$FS = U/\sin\theta \qquad (4)$$

$$S = U/\tan\theta \qquad (5)$$

where U is the uplift rate and θ is the dip angle of the fault plane. We measured the vertical component of the total slip of 45 ± 4 m from the hillslope angle plot derived from the DEM and 41.4 ± 2.2 m from the extrapolated handheld GPS measurements (Figure 7 and Table S1 in the supporting information). Note that because the T3 terrace levels on the hanging wall and the footwall are parallel (the slopes of the linear fits to terrace

Figure 7. Schematic cross section along Baner Khad showing relative heights of terrace and stream profile. Heights of terrace level T3 are obtained from handheld GPS measurements (pink triangles in the main map and profile, and pink points in the regression fit map in the inset) and DEM-derived sample points (red triangles in the main map and profile). Terrace level T3 (10.1 ± 0.9 ka) is extrapolated along the river profile onto a vertical line representing the trace of JMT. The offset of T3 on that line is equal to the differential uplift across the thrust since the formation of T3. With a total vertical offset of 44 ± 5 m, the shortening rate across the Jwalamukhi Thrust is 5.6 ± 0.8 to 7.5 ± 1.1 mm a^{-1} (the calculated shortening and slip rates depend on the dip of the fault plane, as shown in Table 3).

heights on either side of the fault are equal, as shown in Figure 7), it is not necessary to decompose the vertical offset into two components, as is done in *Thompson et al.* [2002] for nonparallel strain markers. We conservatively estimate that the uncertainty on slip across the JMT spans the cumulative range of these two independent measurements, resulting in an offset of 44 ± 5 m [e.g., *Zechar and Frankel*, 2009]. To determine the slip rate, we used the oldest age obtained from terrace level T3, assuming that the younger ages are likely to have been affected by more erosion. Therefore, our shortening rate (*S*) estimate ranges between 5.6 ± 0.8 and 7.5 ± 1.1 mm a^{-1} based on the three different assumed thrust-fault angles (Table 3). Considering that there is a change in the dip of the JMT thrust plane from the flat (10 to 12°) to the ramp (30 to 38°) segment, rock uplift above the ramp segment of JMT is ~3.5 times faster than above the flat segment of the JMT.

Our newly obtained shortening rates of 5.6 ± 0.8 to 7.5 ± 1.1 mm a^{-1} since 10 ka are faster than previously published estimates of 3.5 to 4.2 mm a^{-1} over the last 30 ka by *Thakur et al.* [2014], whose estimates were derived from OSL-dated alluvium lying above the uplifted strath surfaces along the Baner Khad (see previous section). These lower rates might be a result of the older ages used for the deformed terraces, which are derived from the timing of alluvial deposition rather than the timing of terrace abandonment.

4.4. Fluvial Network and Stream Morphometry

All streams originating from the southern flank of the Dhauladhar Range cross the MBT fault zone to enter the Kangra Basin. There, the channels are generally wider and they meander near the southern margin of the basin. Near the southwestern margin of the basin, several streams converge and only two rivers traverse the tilted Upper Siwalik conglomerates via narrow and deeply incised gorges across the hanging wall of the JMT and the BrT. As they flow through the tilted Siwalik units, they are characterized by sudden flow direction shifts from strike perpendicular to strike parallel with respect to the WNW-ESE striking JMT/BrT zones (Figures 3 and 5) before they cross the fault, where individual fault segments of the JMT terminate and/or overlap.

Longitudinal profiles of the streams traversing the JMT and BrT show overall concave upward shapes with k_{sn} values ranging from less than 20 to greater than 150 $m^{0.9}$ (Figure 8a). Stream profiles are marked by breaks in slope and changes in k_{sn} values, which we illustrate with an example (Figure 8b).

All streams show relatively high k_{sn} values in the hanging wall of the JMT. These steep stream segments are 4 to 5 km in length (upstream from the trace of the fault) and are marked by knickpoints (K1) at their upstream ends (Figure 7a). These K1 knickpoints occur in both the Baner and Gaj Khads where they pass through the Upper Siwaliks and enter the Middle Siwaliks.
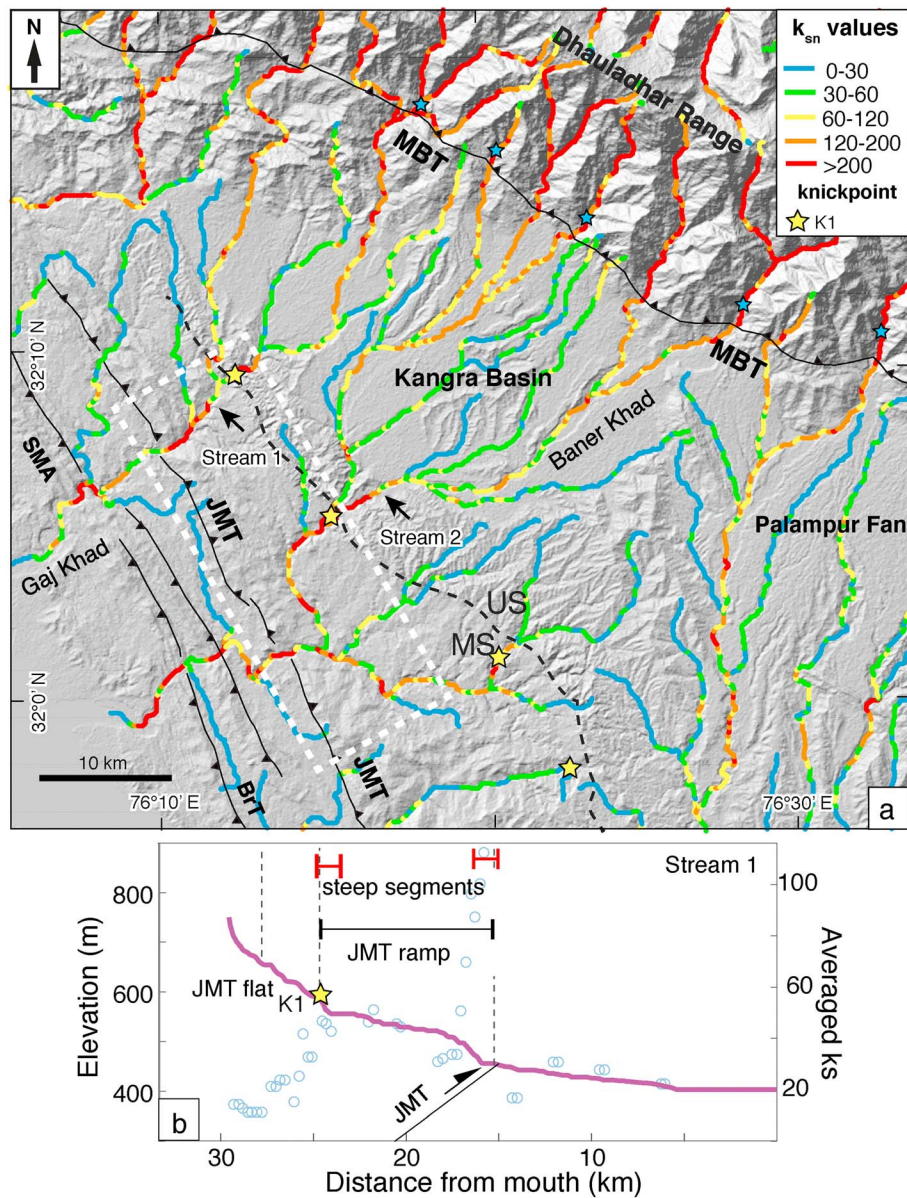
There is a good agreement between changes in the Vfw:Vh ratio with changes in the k_{sn} values (Figure 9). For the Baner Khad, the Vfw:Vh ratio is very low in the Dhauladhar Range (<0.4), but it increases to values of 2 to 4 within the Kangra Basin, and it reaches 5.5 at the southern extremity of the basin (Figure 9). Farther downstream, the ratio falls to 1 when crossing the uplifted Siwalik strata on the hanging wall of the JMT. Similar low ratios are obtained where the river crosses the BrT. Along the Gaj Khad, the Vfw:Vh ratio is higher (3 to 5) within the Kangra basin and drops to values of 2 to 3 where it crosses the uplifted Siwalik strata in the hanging wall of the JMT.

5. Discussion

Our field observations and results from morphometric and exposure age analyses reveal several important aspects of the late Pleistocene-Holocene morphotectonic evolution of the Kangra reentrant. Here we combine our new data on deformation rates and fluvial incision patterns with previously published OSL data (1) to better understand the spatial distribution of deformation across the Sub-Himalaya and (2) to explore potential links between the timing of incision and the occurrence of out-of-sequence deformation within the Kangra reentrant.
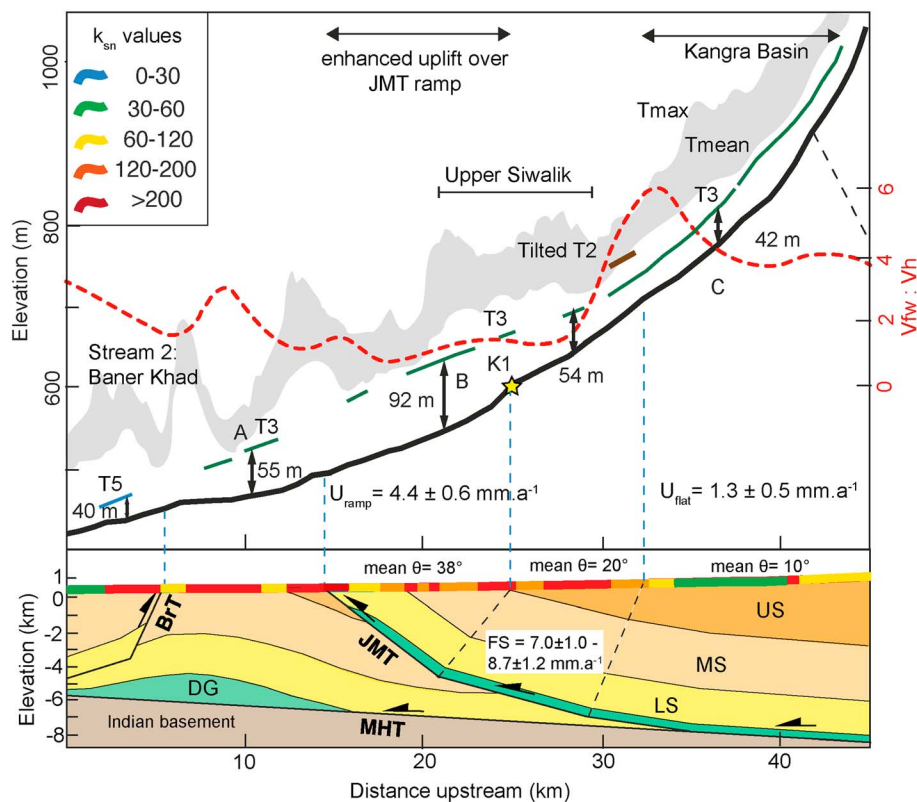
5.1. Activity of the JMT

Previous authors have used field relationships, seismic reflection profiles, balanced cross sections, and uplifted strath terraces to quantify the tectonic activity along the JMT [*Powers et al.*, 1998; *Thakur et al.*, 2014] on different timescales, but the age constraints and therefore rate estimates were limited. *Powers et al.* [1998] proposed that on average, nearly one third of the total Sub-Himalayan shortening (between

Figure 8. (a) Normalized steepness indices map of the study area. Dashed white box highlights zone of relatively high steepness for the stream networks. (b) Stream 1 (from Figure 8a), shows a longitudinal stream profile across the JMT, where knickpoint K1 reflects the transition from flat to ramp on the JMT thrust plane or zone of higher rock uplift.

the PT and the MFT) of $14 \pm 2\,mm\,a^{-1}$ has been accommodated during the Quaternary. However, this is a minimum estimate, as these authors used the approximate timing of cessation of sedimentation of the Upper Siwaliks to constrain the onset of folding and faulting. They inferred an age of 1.9 to 1.6 Ma for the termination of Upper Siwalik sedimentation based on extrapolation of paleomagnetic profiles located ~15 to 20 km east of the study area and assuming a constant sedimentation rate [*Ranga Rao*, 1993]. Therefore, their rate estimates may differ from the actual long-term shortening rate. Revised stratigraphic constraints used by *Hirschmiller et al.* [2014] provide a shortening rate of $8.52 \pm 1.6\,mm\,a^{-1}$ since 2.7 ± 0.3 Ma, also using an interpolated age of the Upper/Middle Siwalik boundary. However, this boundary is likely time transgressive along strike, and the accuracy of the estimate in the Kangra Basin is difficult to assess. Furthermore, as mentioned in section 4.3, the rate estimates from *Thakur et al.* [2014] may underestimate the true deformation rates because their OSL ages likely overestimate the abandonment ages of the deformed terraces.

Figure 9. Longitudinal river profiles along the Baner Khad (stream 2 in Figure 8a) plotted together with terrace profiles, topographic swath (2 km wide swath window; Tmax: maximum topography, Tmean: mean topography), valley-floor width to valley-height ratio (red dashed line, right axis) and normalized steepness indices (k_{sn}). The subsurface geology has been modified after the balanced cross section by *Powers et al.* [1998] and our own field observations. The river profile is characterized by a pronounced knickpoint. We interpret knickpoint K1 to be quasistatic, reflecting differential uplift over segments of the fault with differing dips. Segments undergoing faster uplift are characterized by relatively low Vfw:Vh ratios and relatively high k_{sn} values, even in the Middle-Lower Siwalik sandstone and claystones, which are relatively weak compared to the well-cemented boulder conglomerates of the Upper Siwaliks. Fault slip rate (FS) and uplift rates (U) on the JMT are indicated.

Our new chronologic data and the application of a fault-bend fold model to quantify the deformation in the Sub-Himalaya result in a shortening rate of 5.6 ± 0.8 to 7.5 ± 1.1 mm a^{-1} across the JMT since 10 ± 0.9 ka (the oldest obtained exposure (abandonment) age of terrace level T3), considering a range of different dip angles of the JMT fault plane. In the following sections, we place our findings in the context of deformed fluvial terraces and the observed knickpoints in stream profiles.

5.1.1. Deformation of the Alluvium and Terraces

Srivastava et al. [2009] suggested a rapid late Pleistocene sedimentation phase (<78 ka) in the Kangra Basin, which they related to reactivation of the MBT and some other regional faults. The evidence for this fault reactivation, however, is ambiguous, and the sediment aggradation can alternatively be argued to result from a higher sediment supply due to climatic changes on multimillennial time scales [*Dey et al.,* 2016]. In any case, the angular unconformity between the Siwalik units and the overlying Pleistocene alluvial fill (Figures 4c and 4h) suggest slip on the JMT was ongoing prior to deposition of the late Pleistocene sediments. The presence of a thin veneer of alluvium on top of the tilted Siwaliks in close proximity to the JMT suggests that sediment deposition in the basin surpassed the basin boundary and also occurred downstream.

In addition to the vertical offset of terrace T3 across the JMT (see section 4.3), we also interpret the 12–13° northeast tilted T2 terrace surface (Figure 4h) southwest of the town of Kangra to reflect motion along the MHT. Specifically, we suggest that motion along the fault transported the terrace from an initial position above the flat portion of the MHT onto the first thrust ramp segment along the JMT (Figure 9) after terrace abandonment at ~15.6 ± 1.2 ka.

5.1.2. Morphometric Evidence of Tectonic Activity

Our k_{sn} map (Figure 8a) reveals that streams are characterized by high k_{sn} values ($k_{sn} > 120$) where they cross the JMT hanging wall (above the ramp) and in the 4 to 5 km long reach upstream from the fault trace. Farther upstream, k_{sn} values are lower (<60). Knickpoints marking the upstream end of the high-steepness zone (K1) correspond to lithologic contacts (Figures 3 and 8a), but because this contact is a hard-to-soft transition (partly cemented Upper Siwalik conglomerates are less erodible than the Middle Siwalik sandstones), the K1 knickpoints cannot be lithologically controlled. If they were, the segment downstream from the K1 knickpoints would have lower k_{sn} values compared to the segment upstream from it. Instead, this set of knickpoints more likely reflects the transition from flat to ramp along the JMT thrust and therefore may represent the northern limit of enhanced uplift rates. Therefore, our favored interpretation of the K1 knickpoints is that they are quasistatic, reflecting spatially differential uplift due to changes in the dip of the thrust plane at depth. This interpretation is supported by our field observations: where we have good constraints on the ramp geometry in our field area, the region of higher k_{sn} and low valley-width to valley-height ratio corresponds well to the inferred position of the ramp (Figure 9).

In summary, our fault slip rate estimates, k_{sn} patterns, Vfw:Vh ratios, and field observations such as the back-tilted terrace suggest activity of the JMT since at least 18 ka. Our results provide new and independent estimates of shortening on millennial time scales, which complement the previously proposed long-term average tectonic shortening rates [*Powers et al.*, 1998; *Thakur et al.*, 2014; *Hirschmiller et al.*, 2014]. Whereas the offset terrace allows us to constrain tectonic uplift due to JMT activity, the k_{sn} values on longitudinal stream profiles provide a qualitative estimate of uplift patterns across the entire region. Different segments of the hanging wall of the JMT are expected to have different uplift rates depending on the dip of the thrust plane. Indeed, the ramp segment with higher rock uplift yields higher k_{sn} values and lower Vfw:Vh ratios, whereas the flat segment yields lower k_{sn} values and higher Vfw:Vh ratios. In short, our tectonic rate estimates are supported by our morphometric analyses.

5.2. Importance of Sub-Himalayan Thrusts With Respect To a Critically Tapered Wedge

Previous workers [*Powers et al.*, 1998; *Malik and Mohanty*, 2007; *Thakur et al.*, 2014] have inferred that only the Sub-Himalayan thrusts (JMT, ST, MFT, and related back thrusts) are accommodating modern crustal shortening. Although potential activity on the MBT has been proposed in the NW Himalaya based on ther-mochronology data [*Deeken et al.*, 2011], which would suggest an overall reduced contribution of Sub-Himalayan shortening, the long averaging time scale of thermochronology data makes it difficult to accu-rately assess recent activity. Our morphometric analyses of the reentrant supports these earlier interpreta-tions of the activity of Sub-Himalayan faults, and specifically the JMT (section 4.4). *Thakur et al.* [2014] proposed a shortening rate of 3.5 to 4.2 mm a^{-1} on the JMT over the last 30 ka and 6 to 6.9 mm a^{-1} on the MFT over the last 40 ka. *Powers et al.* [1998] proposed that 25–30% of the total Sub-Himalayan shorten-ing has been accommodated by the JMT. With our new shortening estimates over the last ~10 ka (5.6 ± 0.8 to 7.5 ± 1.1 mm a^{-1}), we show that Holocene shortening on the JMT has been comparable to the activity of the MFT estimated over 30 ka [*Thakur et al.*, 2014]. Present-day geodetic measurements of shortening in the Kangra reentrant have been estimated at 14 ± 2 mm a^{-1} [*Banerjee and Burgmann*, 2002; *Kundu et al.*, 2014] and 13.3 ± 1.7 mm a^{-1} [*Stevens and Avouac*, 2015], whereas underthrusting of the Indian plate has been estimated to be ~4 mm a^{-1} [*Bollinger et al.*, 2004]. Combined with our new results, the data reveal that the JMT accommo-dates ~40–60% of the total convergence across the NW Himalaya at least since the Holocene. Hence, it appears as if the majority of the Holocene shortening has been nearly equally distributed over the JMT and other Sub-Himalayan thrusts (including the MFT) in the Kangra reentrant.

To try to explain why so much Holocene shorting has been accommodated within the interior of the Sub-Himalaya in the form of out-of-sequence faulting, the critically tapered wedge model [*Davis et al.*, 1983] can be considered. In analogue and numerical models of critically tapered wedges, changes in sedimentary load have been shown to influence the location of faulting [*Davis et al.*, 1983]. Sediment aggradation within intermontane valleys or near the front of a wedge can potentially increase the taper and thus induce foreland propagation of deformation to maintain critical taper [*Dahlen*, 1990; *Willett and Beaumont*, 1994; *Hilley and Strecker*, 2004]. Conversely, removal of stored sediments in intermontane basins lower the frontal taper, ren-dering it subcritical, and hence causing the retreat of the deformation front and out-of-sequence thrusting,

until the wedge reestablishes its critical taper [*Dahlen*, 1990]. The applicability of the critical taper model for the whole Himalaya is highly debated and is certainly oversimplified. Nonetheless, it has commonly been used as a first-order framework to explain the tectonic evolution and deformation of the frontal fold-and-thrust belt of the Himalaya, as this region satisfies the mechanical criteria for the evolution of a critical Coulomb wedge [*Hilley and Strecker*, 2004; *Mugnier et al.*, 2004; *Mukul*, 2010; *Singh et al.*, 2012; *Hirschmiller et al.*, 2014].

In this context, the deformation pattern within the Sub-Himalaya may be linked to the history of sediment aggradation and removal in the Kangra reentrant. Considering an initial in-sequence development of the major thrusts within the Kangra reentrant, the JMT must have once been the southernmost deformation front of the Himalayan wedge. With continuous convergence between the Himalaya and the underthrusting Indian plate, new surface-breaking thrusts emerged, extending the MHT décollement toward the foreland. Based on balanced cross sections and seismic profiles, a total shortening of ~23 km over the last 1.6–1.9 Ma within the Sub-Himalaya has been estimated [*Powers et al.*, 1998]. From these cross sections, we can deduce a total shortening on the JMT of 6 to 6.8 km and obtain long-term average shortening rate of 3.6 ± 0.3 mm a^{-1}. From the same balanced cross sections, we can deduce a long-term average slip rate of 0.7 ± 0.2 mm a^{-1} on the MFT. These rates are significantly below slip estimates averaged since the late Pleistocene or Holocene, including those from *Thakur et al.* [2014] and from this study. This inconsistency between short- and long-term slip estimates points to temporal variation of fault activity throughout the last 1.6–1.9 Ma, possibly with periods of low or no activity.

Sediment cycles operate on 10^4–10^5 year timescales and can potentially influence tectonic stress fields by changing the sediment load [*Hilley and Strecker,* 2004, 2005]. Extensive aggradation reaching up to the contiguous foreland around 40–50 ka has been reported by many previous studies [*Gibling et al.*, 2005; *Clift et al.*, 2012; *Thakur et al.*, 2014; *Dey et al.*, 2016]. Late Pleistocene sediment aggradation of more than 200 m across the Kangra Basin (from ~80 to 20 ka) [*Srivastava et al.*, 2009; *Dey et al.*, 2016] spanning more than ~1500 km^2 over the hanging wall of the JMT may have stabilized the critical taper involving the JMT-MHT during times of high loading and therefore forced deformation to localize toward the frontal structures of the wedge. Later, when the transiently stored basin-fill sediments were excavated (only 10–15% of the total volume of sediments stored during full-basin stage remains at present on the hanging wall of JMT), the effective normal stresses on the décollement of the JMT would have been reduced, potentially leading to a subcritical taper [*Singh et al.*, 2012]. By transfer or renewal of out-of-sequence fault activity to inherited structures such as the JMT within the Kangra reentrant, the critical taper would have been restored. Although detailed modeling is necessary to test these ideas in detail, the coincidence in the timing of sediment excavation from the Kangra Basin with an apparent increase in slip rate along the JMT provides a compelling argument for linking the two events in the context of a critically tapered wedge.

6. Conclusions

Within the Kangra intermontane basin, deformation of well-preserved Holocene terraces indicates neotectonic activity along the Jwalamukhi Thrust (JMT). The basin hosts evidence for at least two aggradation and incision sedimentary cycles during late Pleistocene to Holocene times. The latest of these aggradation periods was succeeded by episodic reincision and terrace abandonment, creating at least four terrace levels (T3-T6) during the Holocene, the oldest and best preserved of which (T3) was formed at 10.1 ± 0.9 ka. Differential uplift of 44 ± 5 m of the best preserved terrace level (T3) across the JMT suggests out-of-sequence faulting along the JMT and yields a shortening rate of 5.6 ± 0.8 to 7.5 ± 1.1 mm a^{-1} over the last ~10 kyr. In the context of recently published shortening rates averaged over the past ~2 Myr [*Powers et al.*, 1998] and 30 to 40 ka [*Thakur et al.*, 2014], as well as GPS-derived shortening rates [*Kundu et al.*, 2014], our results suggest that a significant proportion of the shortening has been accommodated by the JMT over the Holocene. This shortening corresponds to about 40 to 60% of the total Sub-Himalayan shortening, or 30 to 50% of the total convergence accommodated within the Himalaya. We propose that the recent out-of-sequence faulting that we document along the JMT is potentially related to a tectonic reorganization triggered by temporal variations in sedimentary loading within the toe area of the Himalayan orogenic wedge.

References

Ader, T., et al. (2012), Convergence rate across the Nepal Himalaya and interseismic coupling on the Main Himalayan Thrust: Implications for seismic hazard, *J. Geophys. Res.*, *117*, B04403, doi:10.1029/2011JB009071.

Avouac, J., and P. Tapponnier (1993), Kinematic model of active deformation in central Asia, *Geophys. Res. Lett.*, *20*, 895–898, doi:10.1029/93GL00128.

Banerjee, P., and R. Burgmann (2002), Convergence across the northwest Himalaya from GPS measurements, *Geophys. Res. Lett.*, *29*(13), 1652, doi:10.1029/2002GL015184.

Balco, G., J. O. Stone, N. A. Lifton, T. J. Dunai (2008), A complete and easily accessible means of calculating surface exposure ages or erosion rates from (10)Be and (26)Al measurements, *Quat. Geochronol.*, *3*, 174–195, doi:10.1016/j.quageo.2007.12.001.

Bettinelli, P., J. P. Avouac, M. Flouzat, F. Jouanne, L. Bollinger, P. Willis, and G. R. Chitrakar (2006), Plate motion of India and interseismic strain in the Nepal Himalaya from GPS and DORIS measurements, *J. Geod.*, *80*(8–11), 567–589.

Bollinger, L., J. P. Avouac, R. Cattin, and M. R. Pandey (2004), Stress buildup in the Himalaya, *J. Geophys. Res.*, *109*, B11405, doi:10.1029/2003JB002911.

Borchers, B., S. Marrero, G. Balco, M. Caffee, B. Goehring, N. Lifton, K. Nishiizumi, F. Phillips, J. Schaefer, and J. Stone (2016), Geological calibration of spallation production rates in the CRONUS-Earth project, *Quat. Geochronol.*, *31*, 188–198.

Brocard, G. Y., P. A. Van Der Beek, D. L. Bourlès, L. L. Siame, and J.-L. Mugnier (2003), Long-term fluvial incision rates and postglacial river relaxation time in the French Western Alps from ^{10}Be dating of alluvial terraces with assessment of inheritance, soil development and wind ablation effects, *Earth Planet. Sci. Lett.*, *209*(1), 197–214.

Brozovic, N., and D. W. Burbank (2000), Dynamic fluvial systems and gravel progradation in the Himalayan foreland, *Geol. Soc. Am. Bull.*, *112*(3), 394–412, doi:10.1130/0016-7606(2000)112<0394:dfsagp>2.3.co;2.

Bull, W. B. (2008), *Tectonic Geomorphology of Mountains: A New Approach to Paleoseismology*, John Wiley, Malden, Mass.

Burbank, D. W., and R. G. H. Raynolds (1988), Stratigraphic keys to the timing of thrusting in terrestrial foreland basins: Applications to the northwestern Himalaya, in *New Perspectives in Basin Analysis*, pp. 331–351 , Springer, New York.

Clift, P. D., et al. (2012), U-Pb zircon dating evidence for a Pleistocene Sarasvati River and capture of the Yamuna River, *Geology*, *40*(3), 211–214.

Dahlen, F. (1990), Critical taper model of fold-and-thrust belts and accretionary wedges, *Annu. Rev. Earth Planet. Sci.*, *18*(1), 55–99, doi:10.1146/annurev.earth.18.1.55.

Davis, D., J. Suppe, and F. A. Dahlen (1983), Mechanics of fold-and-thrust belts and accretionary wedges, *J. Geophys. Res.*, *88*(B2), 1153–1172, doi:10.1029/JB088iB02p01153.

DeCelles, P. G., D. M. Robinson, J. Quade, T. P. Ojha, C. N. Garzione, P. Copeland, and B. N. Upreti (2001), Stratigraphy, structure, and tectonic evolution of the Himalayan fold-thrust belt in western Nepal, *Tectonics*, *20*, 487–509, doi:10.1029/2000TC001226.

Deeken, A., R. C. Thiede, E. R. Sobel, J. K. Hourigan, and M. R. Strecker (2011), Exhumation variability within the Himalaya of northwest India, *Earth Planet. Sci. Lett.*, *305*(1–2), 103–114, doi:10.1016/j.epsl.2011.02.045.

Dewald, A., et al. (2013), Cologne AMS, a dedicated center for accelerator mass spectrometry in Germany, *Nucl. Instruments Methods Phys. Res. Sect. B Beam Interact.Mater. Atoms*, *294*, 18–23, doi:10.1016/j.nimb.2012.04.030.

Dey, S., R. C. Thiede, T. F. Schildgen, H. Wittmann, D. Scherler, B. Bookhagen, V. Jain, and M. R. Strecker (2016), Climate-driven sediment aggradation and incision since the late Pleistocene in the NW Sub-Himalaya, India, *Earth Planet. Sci. Lett.*, doi:10.1016/j.epsl.2016.05.050.

Dunne, J., D. Elmore, and P. Muzikar (1999), Scaling factors for the rates of production of cosmogenic nuclides for geometric shielding and attenuation at depth on sloped surfaces, *Geomorphology*, *27*(1), 3–11.

Duvall, A., E. Kirby, and D. Burbank (2004), Tectonic and lithologic controls on bedrock channel profiles and processes in coastal California, *J. Geophys. Res.*, *109*, F03002, doi:10.1029/2003JF000086.

Flint, R. F. (1974), Three theories in time, *Quat. Res.*, *4*(1), 1–8, doi:10.1016/0033-5894(74)90059-3.

Gansser, A. (1964), *Geology of the Himalayas*, Intersci. Publ., New York.

Gibling, M. R., S. K. Tandon, R. Sinha, and M. Jain (2005), Discontinuity-bounded alluvial sequences of the southern gangetic plains, India: Aggradation and degradation in response to monsoonal strength, *J. Sediment. Res.*, *75*(3), 369–385, doi:10.2110/jsr.2005.029.

Hidy, A. J., J. C. Gosse, J. L. Pederson, J. P. Mattern, and R. C. Finkel (2010), A geologically constrained Monte Carlo approach to modeling exposure ages from profiles of cosmogenic nuclides: An example from Lees Ferry, Arizona, *Geochem. Geophys. Geosyst.*, *11*, Q0AA10, doi:10.1029/2010GC003084.

Hilley, G. E., and M. R. Strecker (2004), Steady state erosion of critical Coulomb wedges with applications to Taiwan and the Himalaya, *J. Geophys. Res.*, *109*, B01411, doi:10.1029/2002JB002284.

Hilley, G. E., and M. R. Strecker (2005), Processes of oscillatory basin filling and excavation in a tectonically active orogen: Quebrada del Toro Basin, NW Argentina, *Geol. Soc. Am. Bull.*, *117*(7–8), 887–901, doi:10.1130/b25602.1.

Hirschmiller, J., D. Grujic, B. Bookhagen, I. Coutand, P. Huyghe, J.-L. Mugnier, and T. Ojha (2014), What controls the growth of the Himalayan foreland fold-and-thrust belt?, *Geology*, *42*(3), 247–250, doi:10.1130/g35057.1.

Jouanne, F., J. L. Mugnier, J. F. Gamond, P. Le Fort, M. R. Pandey, L. Bollinger, M. Flouzat, and J. P. Avouac (2004), Current shortening across the Himalayas of Nepal, *Geophys. J. Int.*, *157*(1), 1–14.

Kumar, R., N. Suresh, S. J. Sangode, and V. Kumaravel (2007), Evolution of the Quaternary alluvial fan system in the Himalayan foreland basin: Implications for tectonic and climatic decoupling, *Quat. Int.*, *159*, 6–20, doi:10.1016/j.quaint.2006.08.010.

Kundu, B., R. K. Yadav, B. S. Bali, S. Chowdhury, and V. K. Gahalaut (2014), Oblique convergence and slip partitioning in the NW Himalaya: Implications from GPS measurements, *Tectonics*, *33*, 2013–2024, doi:10.1002/2014tc003633.

Lal, D. (1991), Cosmic ray labeling of erosion surfaces: In situ nuclide production rates and erosion models, *Earth Planet. Sci. Lett.*, *104*, 424–439.

Lave, J., and J. P. Avouac (2000), Active folding of fluvial terraces across the Siwaliks Hills, Himalayas of central Nepal, *J. Geophys. Res.*, *105*, 5735–5770, doi:10.1029/1999JB900292.

Lyon-Caen, H., and P. Molnar (1985), Gravity anomalies, flexure of Indian plate and the structure, support, and evolution of the Himalayan Ganga basin, *Tectonics*, *4*, 513–538, doi:10.1029/TC004i006p00513.

Malik, J. N., and C. Mohanty (2007), Active tectonic influence on the evolution of drainage and landscape: Geomorphic signatures from frontal and hinterland areas along the Northwestern Himalaya, India, *J. Asian Earth Sci.*, *29*(5–6), 604–618, doi:10.1016/j.jseaes.2006.03.010.

Marrero, S. M., F. M. Phillips, B. Borchers, N. Lifton, R. Aumer, and G. Balco (2016), Cosmogenic nuclide systematics and the CRONUScalc program, *Quat. Geochronol.*, *31*, 160–187.

Miller, T. K. (1991), A model of stream channel adjustment: Assessment of Rubey's hypothesis, *J. Geol.*, *99*(5), 699–710.

Mugnier, J.-L., P. Huyghe, P. Leturmy, and F. Jouanne (2004), Episodicity and rates of thrust-sheet motion in the Himalayas (western Nepal), in *Thrust Tectonics and Hydrocarbon Systems*, edited by K. R. McClay, *AAPG Mem.*, 82, 91–114.

Mukhopadhyay, D. K., and P. Mishra (1999), A balanced cross section across the Himalayan foreland belt, the Punjab and Himachal foothills: A reinterpretation of structural styles and evolution, *Proc. Indian Acad. Sci. Planet. Sci.*, 108(3), 189–205.

Mukul, M. (2010), First-order kinematics of wedge-scale active Himalayan deformation: Insights from Darjiling-Sikkim-Tibet (DaSiT) wedge, *J. Asian Earth Sci.*, 39(6), 645–657.

Mukul, M., M. Jaiswal, and A. K. Singhvi (2007), Timing of recent out-of-sequence active deformation in the frontal Himalayan wedge: Insights from the Darjiling sub-Himalaya, India, *Geology*, 35(11), 999–1002, doi:10.1130/g23869a.1.

Nábělek, J., G. Hetényi, J. Vergne, S. Sapkota, B. Kafle, M. Jiang, H. Su, J. Chen, B.-S. Huang, and Hi-Climb Team (2009), Underplating in the Himalaya-Tibet Collision Zone Revealed by the Hi-CLIMB Experiment, *Science*, 325(5946), 1371–1374.

Ni, J., and M. Barazangi (1984), Seismotectonics of the Himalayan Collision Zone: Geometry of the underthrusting Indian Plate beneath the Himalaya, *J. Geophys. Res.*, 89, 1147–1163, doi:10.1029/JB089iB02p01147.

Pavlis, T. L., M. W. Hamburger, and G. L. Pavlis (1997), Erosional processes as a control on the structural evolution of an actively deforming fold and thrust belt: An example from the Pamir-Tien Shan region, central Asia, *Tectonics*, 16, 810–822, doi:10.1029/97TC01414.

Pingel, H., M. R. Strecker, R. N. Alonso, and A. K. Schmitt (2013), Neotectonic basin and landscape evolution in the Eastern Cordillera of NW Argentina, Humahuaca Basin (~ 24 S), *Basin Res.*, 25(5), 554–573.

Pinter, N., and E. A. Keller (1995), Geomorphological analysis of neotectonic deformation, northern Owens Valley, California, *Geol. Rundschau*, 84(1), 200–212, doi:10.1007/BF00192251.

Powers, P. M., R. J. Lillie, and R. S. Yeats (1998), Structure and shortening of the Kangra and Dehra Dun reentrants, sub-Himalaya, India, *Geol. Soc. Am. Bull.*, 110(8), 1010–1027, doi:10.1130/0016-7606(1998)110<1010:sasotk>2.3.co;2.

Prasad, B. R., S. L. Klemperer, V. V. Rao, H. C. Tewari, and P. Khare (2011), Crustal structure beneath the Sub-Himalayan fold–thrust belt, Kangra recess, northwest India, from seismic reflection profiling: Implications for Late Paleoproterozoic orogenesis and modern earthquake hazard, *Earth Planet. Sci. Lett.*, 308(1), 218–228.

Raiverman, V., D. N. Prasad, and A. K. Srivastava (1994), Structural style in northwestern Himalayan foothills, *Himalaya Geol.*, 15, 263–280.

Ranga Rao, A. (1993), Magnetic-polarity stratigraphy of Upper Siwalik of north-western Himalayan foothills, *Curr. Sci.*, 64(11–12), 863–873.

Repka, J. L., R. S. Anderson, and R. C. Finkel (1997), Cosmogenic dating of fluvial terraces, Fremont River, Utah, *Earth Planet. Sci. Lett.*, 152(1–4), 59–73, doi:10.1016/s0012-821x(97)00149-0.

Sah, M. P., and R. A. K. Srivastava (1992), Morphology and facies of the alluvial-fan sedimentation in the Kangra Valley, Himachal Himalaya, *Sediment. Geol.*, 76(1–2), 23–42, doi:10.1016/0037-0738(92)90137-G.

Schaller, M., T. A. Ehlers, J. D. Blum, and M. A. Kallenberg (2009), Quantifying glacial moraine age, denudation, and soil mixing with cosmogenic nuclide depth profiles, *J. Geophys. Res.*, 114, F01012, doi:10.1029/2007JF000921.

Schildgen, T. F., D. Cosentino, B. Bookhagen, S. Niedermann, C. Yildirim, H. Echtler, H. Wittmann, and M. R. Strecker (2012), Multi-phased uplift of the southern margin of the Central Anatolian plateau, Turkey: A record of tectonic and upper mantle processes, *Earth Planet. Sci. Lett.*, 317–318, 85–95.

Schwanghart, W., and D. Scherler (2014), TopoToolbox 2—MATLAB-based software for topographic analysis and modeling in Earth surface sciences, *Earth Surf. Dyn.*, 2, 1–7.

Shreve, R. L. (1968), Leakage and fluidization in air-layer lubricated avalanches, *Geol. Soc. Am. Bull.*, 79(5), 653, doi:10.1130/0016-7606(1968)79[653:lafial]2.0.co;2.

Singh, T., A. K. Awasthi, and R. Caputo (2012), The sub-Himalayan fold-thrust belt in the 1905 Kangra earthquake zone: A critical taper model perspective for seismic hazard analysis, *Tectonics*, 31, TC6002, doi:10.1029/2012TC003120.

Snyder, N. P., K. X. Whipple, G. E. Tucker, and D. J. Merritts (2000), Landscape response to tectonic forcing: Digital elevation model analysis of stream profiles in the Mendocino triple junction region, northern California, *Geol. Soc. Am. Bull.*, 112(8), 1250–1263, doi:10.1130/0016-7606(2000)112<1250:lrttfd>2.3.co;2.

Srivastava, P., M. K. Rajak, and L. P. Singh (2009), Late Quaternary alluvial fans and paleosols of the Kangra basin, NW Himalaya: Tectonic and paleoclimatic implications, *Catena*, 76(2), 135–154, doi:10.1016/j.catena.2008.10.004.

Steck, A. (2003), Geology of the NW Indian Himalaya, *Eclogae Geol. Helv.*, 96, 147–U13, doi:10.1007/s00015-003-1091-4.

Stevens, V. L., and J. P. Avouac (2015), Interseismic coupling on the main Himalayan thrust, *Geophys. Res. Lett.*, 42, 5828–5837, doi:10.1002/2015GL064845.

Stone, J. O. (2000), Air pressure and cosmogenic isotope production, *J. Geophys. Res.*, 105, 23,753–23,759, doi:10.1029/2000JB900181.

Thakur, V. C., A. K. Pandey, and N. Suresh (2007), Late Quaternary-Holocene evolution of Dun structure and the Himalayan Frontal Fault zone of the Garhwal Sub-Himalaya, NW India, *J. Asian Earth Sci.*, 29(2–3), 305–319, doi:10.1016/j.jseaes.2006.02.002.

Thakur, V. C., M. Joshi, D. Sahoo, N. Suresh, R. Jayangondapermal, and A. Singh (2014), Partitioning of convergence in Northwest Sub-Himalaya: Estimation of late Quaternary uplift and convergence rates across the Kangra reentrant, North India, *Int. J. Earth Sci.*, 103(4), 1037–1056, doi:10.1007/s00531-014-1016-7.

Thompson, S. C., R. J. Weldon, C. M. Rubin, K. Abdrakhmatov, P. Molnar, and G. W. Berger (2002), Late Quaternary slip rates across the central Tien Shan, Kyrgyzstan, central Asia, *J. Geophys. Res.*, 107(B9), 2203, doi:10.1029/2001JB000596.

Wesnousky, S. G., S. Kumar, R. Mohindra, and V. C. Thakur (1999), Uplift and convergence along the Himalayan frontal thrust of India, *Tectonics*, 18, 967–976, doi:10.1029/1999TC900026.

Whipple, K. X., and G. E. Tucker (1999), Dynamics of the stream-power river incision model: Implications for height limits of mountain ranges, landscape response timescales, and research needs, *J. Geophys. Res.*, 104, 17,661–17,674, doi:10.1029/1999JB900120.

Willett, S. D., and C. Beaumont (1994), Subduction of Asian lithospheric mantle beneath Tibet inferred from models of continental collision, *Nature*, 369(6482), 642–645.

Wobus, C., A. M. Heimsath, K. Whipple, and K. V. Hodges (2005), Active out-of-sequence thrust faulting in the central Nepalese Himalaya, *Nature*, 434(7036), 1008–1011.

Wobus, C. W., G. E. Tucker, and R. S. Anderson (2006), Self-formed bedrock channels, *Geophys. Res. Lett.*, 33, L18408, doi:10.1029/2006GL027182.

Zechar, J. D., and K. L. Frankel (2009), Incorporating and reporting uncertainties in fault slip rates, *J. Geophys. Res.*, 114, B12407, doi:10.1029/2009JB006325.